Parvalbumin-producing Striatal Interneurons Received Excitatory Inputs onto Proximal Dendrites from Motor Thalamus in Male Mice

DOCTORAL DISSERTATION

By:

Yasutake Nakano

Supervisor:

Dr. Fumino Fujiyama

Co-Supervisor:

Dr. Fuyuki Karube

Graduate School of Brain Science

Doshisha University

March 2018

Kyoto, Japan

Abstract

In rodents, the dorsolateral striatum regulates voluntary movement by integrating excitatory inputs from the motor-related cerebral cortex and thalamus to produce contingent inhibitory output to other basal ganglia nuclei. Striatal parvalbumin (PV)-producing interneurons receiving this excitatory input then inhibit medium spiny neurons (MSNs) and modify their outputs. To understand basal ganglia function in motor control, it is important to reveal the precise synaptic organization of motor-related cortical and thalamic inputs to striatal PV interneurons. To examine which domains of the PV neurons receive these excitatory inputs, we used male BAC transgenic mice that expressed somatodendritic membrane-targeted GFP in PV neurons. Anterograde tracing study with the adeno-associated virus vector combined with immunodetection of pre- and post-synaptic markers visualized the distribution of the excitatory appositions on PV dendrites. Statistical analysis revealed that the density of thalamostriatal appositions along the dendrites was significantly higher on the proximal than distal dendrites. In contrast, there was no positional preference in the density of appositions from axons of dorsofrontal cortex. Population observations of thalamostriatal and corticostriatal appositions by immunohistochemistry for pathway-specific vesicular glutamate transporters confirmed that thalamic inputs preferentially, and cortical ones less preferentially, made apposition on proximal dendrites of PV neurons. This axodendritic organization suggests that PV neurons produce fast and reliable inhibition of MSNs in response to thalamic inputs and process excitatory inputs from motor cortices locally and plastically, possibly

together with other GABAergic and dopaminergic dendritic inputs, to modulate MSN

inhibition.

Abbreviations

AAV, adeno-associated virus; AD, anterodorsal thalamic nucleus; AM, anteromedial thalamic nucleus; Ang, angular thalamic nucleus; AV, anteroventral thalamic nucleus; CS, corticostriatal; Cx, cortex; DCN, deep cerebellar nuclei; EP, entopeduncular nucleus; EPSC, excitatory postsynaptic current; EZ, excitatory subcortical afferent-dominant zone; fAHP, after-hyperpolarization; IL, intralaminar thalamic nuclei; ISI, interspike interval; IZ, inhibitory afferent-dominant zone; LD, laterodorsal thalamic nucleus; LM, lateromedial; LP, lateral posterior thalamic nucleus; M1, primary motor cortex; M2, secondary motor cortex; ML, midline thalamic nuclei; MSN, medium spiny neuron; NGF, neurogliaform; NPY, neuropeptide Y; OPC, oval paracentral thalamic nucleus; PaF, parafascicular thalamic nucleus; PC, paracentral thalamic nucleus; Po, posterior thalamic nuclear group; PSD95, postsynaptic density 95; PV, parvalbumin; ROI, region of interest; Rt, reticular nucleus (prethalamus); Rt, reticular nucleus; SD, standard deviation; SNr, substantia nigra pars reticulata; SOM, somatostatin; str, striatum; TS, thalamostriatal; VA, ventral anterior nucleus; VA/VL, ventral anterior/ventral lateral complex; VGluT1, vesicular glutamate transporter 1; VGluT2, vesicular glutamate transporter 2; VL, ventral lateral nucleus; VM, ventral medial nucleus; VM, ventromedial thalamic nucleus; VPM, ventral posteromedial thalamic nucleus; VPPC, ventral posterior nucleus of the thalamus parvicellular.

Acknowledgement

Table of contents

3. Result

4. Discussion

5. Reference 62

List of Figures and Tables

Figures

Tables

1. Introduction

1.1. Cortico-basal ganlia-thalamo-cortical loop

Fig.1: Convergence of motor related cortex and thalamus into the striatum. Rostromeial VA/VL receives input from the output nuclei of the basal ganglia and directly project to the striatum.

Basal ganglia are involved in motor function. The basal ganglia constitute loop circuits with cerebral cortex and thalamus (Alexander et al., 1986). The striatum, which is input nucleus of the basal ganglia, receives massive input from motor area of cerebral cortex. Output nuclei of the basal ganglia are entopeduncular nucleus (EP) and subtantia nigra pars reticulata (SNr). These nuclei inhibit rostromedial area of ventral anterior / ventral lateral (VA/VL) complex in the thalamus. On the other hand, caudolateral area of VA/VL receives excitatory inputs from the deep cerebellar nuclei (DCN). Both of the rostromedial and caudolateral VA/VL project to motor area of cerebral cortex. The rostromedial VA/VL neurons also send axon collaterals into the striatum (Kuramoto et al., 2009), which is the input nucleus of the basal ganglia. Therefore, the motor-related information from the cortex and thalamus converge in

1

the striatum. In the present study, we investigate how striatum receive the excitatory afferents from VA/VL and cerebral cortex to clarify the way of motor processing in cortico-basal ganglia-thalamic loop.

1.2. Corticostriatal projection and motor function

To process information received from different areas of the cerebral cortex, the striatum utilizes separate functional territories for prefrontal, limbic, oculomotor, and sensorimotor inputs (Alexander et al., 1986; Hikosaka et al., 2000). The primary, supplementary, premotor, and cingulate motor areas project to the dorsal "motor" striatum, including the dorsal postcommissural putamen, and dorsolateral head of the caudate (Kunishio and Haber, 1994; Parent and Hazrati, 1995; Voorn et al., 2004), with each pathway mediating different aspects of motor control (Alexander and Crutcher, 1990; Hikosaka et al., 2002; Graybiel, 2005; Doyon et al., 2009).

1.3. Motor thalamus and thalamostriatal projection

The striatum also receives glutamatergic afferents from thalamus (Smith & Bolam, 1990). This thalamostriatal projection is highly heterogeneous, originating in many thalamic subnuclei including the midline (ML) and intralaminar (IL) thalamic nuclei (Bentivoglio et al., 1991; Groenewegen and Berendse, 1994; Mengual et al., 1999; Van Der Werf et al.,

2002; Unzai et al., 2015). The ventral motor thalamic nuclei, consisting of VA, VL, and ventral medial (VM) nuclei, are another major source of inputs to the striatum (Beckstead, 1984; Smith and Parent, 1986; McFarland and Haber, 2001; Smith et al., 2004; Kuramoto et al., 2009; Kuramoto et al., 2015). In rat brain, the VA and VL constitute a single nuclear mass as the VA-VL complex (Jones, 2007). Since the VA-VL complex receives massive glutamatergic and GABAergic afferents from the cerebellum and basal ganglia, respectively, the topography of the VA-VL complex is defined with the type 2 vesicular glutamate transporter (VGluT2) and glutamic acid decarboxylase (GAD) immunoreactivity as excitatory subcortical afferent-dominant zone (EZ) and inhibitory afferent-dominant zone (IZ) (Kuramoto et al., 2009; Kuramoto et al., 2011). On the other hand, VM receives both the excitatory afferents from cerebellar nuclei and the inhibitory afferents from the basal ganglia without any topography. Single-neuron tracing studies revealed that the axon collaterals originating from both IZ of VA-VL complex and VM directly projected to the striatum, and EZ of VA-VL complex projected to cortex without collaterals in the striatum (Kuramoto et al., 2009; Kuramoto et al., 2015). Thus, the dorsal striatum might receive two kinds of the information originating from the motor thalamus and the motor cortex. In addition, these two striatal projection sources are reciprocally connected, and thus their activities might affect each other via corticothalamic and thalamocortical connections. Therefore, the projection pathway to the striatum is a complex system. In other words, the striatum integrates both

3

information, and thus, it would be important to uncover differences between these synaptic connections.

1.4. Thalamostriatal and corticostriatal synaptic organization

The relationships between ventral motor thalamostriatal and corticostriatal projections from motor, premotor, and supplementary motor areas at the level of the striatum have been demonstrated in the striatum of monkeys (Kunishio and Haber, 1994; Parent and Hazrati, 1995; McFarland and Haber, 2000; McFarland and Haber, 2001; Haber and Mcfarland, 2001) and rats (Inase et al., 1996; Takada et al., 1998). Although there is study-to-study variation in synaptology, a greater proportion of cortical projections make axospinous contacts onto dendrites of medium spiny neurons (MSNs) compared to thalamic projections in all mammal groups (Kemp and Powell, 1971; Hattori et al., 1979; Frotscher et al., 1981; Somogyi et al., 1981; Dubé et al., 1988; Xu et al., 1989; Wilson et al., 1990; Sadikot et al., 1992; Smith et al., 1994; Hersch et al., 1995; Fujiyama et al., 2006; Raju et al., 2006; Lacey et al., 2005; Lacey et al., 2007; Lei et al., 2013). In addition, functional studies suggest that corticostriatal and thalamostriatal axons differ in their electrophysiological modulatory properties (Smeal et al., 2007; Ding et al., 2008; Sciamanna et al., 2015).

1.5. Parvalbumin neurons in striatum

The mammalian striatum consists mainly of MSNs, which account for approximately 85% of the total cell population but also contains two major classes of neurochemically distinct interneurons: cholinergic neurons and GABAergic neurons. The latter class are further divided into subpopulations: GABAergic neurons expressing parvalbumin (PV) and/or serotonin (5HT) receptor 3a, somatostatin (SOM)/nitric oxide synthase (NOS), or calretinin (CR) (Vincent et al., 1983; Vincent and Johansson, 1983; Kita et al., 1990; Cowan et al., 1990; Bennett and Bolam, 1993; Kubota and Kawaguchi, 1993; Kubota et al., 1993; Kubota and Kawaguchi, 1994; Kubota and Kawaguchi, 2000; Tepper and Bolam, 2004; Tepper et al., 2010; Muñoz-Manchado et al., 2016). The cortex and thalamus provide excitatory innervation to both MSNs and striatal interneurons (Sidibe and Smith, 1999; Smith et al., 2004). The MSNs are strongly regulated by striatal interneurons, especially PV neurons, which are the most numerous of striatal interneurons (Kubota and Kawaguchi, 2000; Koos et al., 2004; Gittis et al., 2010; Planert et al., 2010). To better understand how PV neurons regulate striatal output from MSN, it is, therefore, crucial to investigate how the PV neurons are innervated by the cortex and thalamus. PV neurons receive excitatory inputs from the cerebral cortex and IL (Bennett and Bolam, 1993), thus at least non-motor thalamic inputs and cortical inputs could be converged. In addition, Ramanathan et al. (2002) reported that the cortical afferents from the primary motor (M1) and primary somatosensory (S1) areas, namely inputs from multiple

cortical area, also converged on the PV immunopositive neurons. However, the precise organization of cortical and thalamic synapses onto PV neurons is still unclear. In the present study, we addressed this question by providing a quantitative and comprehensive description of how the PV expressing neurons in the dorsal striatum receive motor-related cortical and thalamic inputs. To visualize the entire dendrites of PV producing striatal interneurons, we used bacterial artificial chromosome (BAC) transgenic mice expressing somatodendritic membrane-targeted green fluorescent protein (GFP) (myrGFP-LDLRct), specifically in PV-producing neurons (Kameda et al., 2008; Kameda et al., 2012). The myrGFP-LDLRct is composed of the myristoylation/palmitoylation site of the Fyn N-terminus, GFP, and the C-terminus of the low-density lipoprotein receptor (LDLRct), which is useful for expressing GFP in neuronal somata and dendritic membranes (Kameda et al., 2008). We injected an adeno-associated virus (AAV) expressing tdTomato into the secondary motor area (M2) cortex or VA-VL complex of the thalamus to separately visualize corticostriatal and thalamostriatal axon terminals. To confirm whether AAV labeled axon terminals are actually corticostriatal or thalamostriatal, we used the immunoreactivities for VGluT1 and VGluT2. VGluT1 is predominantly expressed by telencephalic/cortical neurons, whereas VGluT2 is mainly produced by neurons in diencephalic and lower brainstem regions, including thalamus (See Discussion part; for review, see Kaneko et al., 2002; Kaneko and Fujiyama, 2002; Fremeau et al., 2004). Analyses of the organization of striatal excitatory inputs may provide

6

insights how the PV expressing neurons process the cortical and thalamic excitatory afferents

inputs to inhibit MSNs.

2. Materials and Methods

All animal experiments were approved and performed in accordance with the guidelines for the care and use of laboratory animals established by the Committee for Animal Care and Use and that for Recombinant DNA Study of Doshisha University. All efforts were made to minimize animal suffering and the number of animals used. All mice were maintained in the animal breeding facilities at Doshisha University. Chemicals were purchased from Nacalai Tesque (Kyoto, Japan) and Wako (Osaka, Japan) unless otherwise noted.

2.1. Animals and Surgery

In the present study, all experiments were conducted in a transgenic mouse line, called PV-FGL, in which the expression of myrGFP-LDLRct is controlled by the promoter of PV gene (Kameda et al., 2012). Thus, only PV-expressing neurons are labeled by GFP. PV-FGL mice were maintained by crossing male PV-FGL mice with wild-type female mice (C57BL/6J obtained from Japan SLC Inc., Hamamatsu, Japan). Males and females were separated at postnatal (P) week 4. The genotypes of the offspring were verified by polymerase chain reaction using tail DNA. Male PV-FGL mice at P12−P28 weeks (N = 10) were anesthetized by inhalation of isoflurane (Pfizer Japan Inc., Tokyo, Japan) followed by intramuscular injection of mixture of ketamine (Ketalar; Daiichi-Sankyo, Tokyo, Japan; 40 mg/kg) and xylazine (Bayer HealthCare, Tokyo, Japan; 4 mg/kg). Each mouse was then

fixed to a stereotaxic device (Narishige, Tokyo, Japan), and the skull was drilled to make a small hole for injections positioned according to the mouse brain atlas of Paxinos and Flanklin (2013). For cortical or thalamic neuron axon labeling, 0.1 to 0.5 µL of AAV (1.5 × 10^{10} vg/µL AAVdj-CAG-hChR2-H134R-tdTomato; Addgene plasmid #28017; Mao et al., 2011) in phosphate buffered saline (PBS, pH 7.4) was injected into M2 or VA/VL [for M2; anteroposterior (AP): 2.80 mm rostral from the bregma, lateromedial (LM): 1.08 mm lateral from the midline, depth: 0.5, 1.0, and 1.5 mm from the pial surface, respectively, for VA/VL; AP: 1.20 mm caudal from the bregma, LM: 0.96 mm lateral from the midline, depth: 3.8 mm from the pial surface, respectively] using a glass pipette (tip diameter, 10–20 µm). Injection was controlled by air pressure delivered with a pressure injector (PV820, World Precision Instruments, Sarasota, FL). After surgery, the mouse was kept on a temperature control blanket (BWT100A, Bio Research Center, Nagoya, Japan) until recovery from anesthesia and then returned to the home cage. Two of the 10 mice were excluded from this study due to poor neuronal labeling. Each mouse was perfused with fixatives at least 2 weeks after AAV injection, and the tissues were prepared as described below.

2.2. Double or Triple immunofluorescence labeling

Male PV-FGL mice (P19−P22 weeks, N = 5) were deeply anesthetized with isoflurane and sodium pentobarbital (100 mg/kg, i.p.; Kyoritsu Seiyaku Corporation, Tokyo, Japan). Mice were then transcardially perfused with 8.5% sucrose in 20 mM phosphate buffer (PB, pH 7.4) containing 1 mM $MgCl_2$, followed by 4% w/v paraformaldehyde and 75% saturated picric acid in 0.1 M PB. After turning the perfusion pump off, the brain was postfixed in situ for 1.5 h at room temperature (RT), and then the brain was removed from the skull followed by cryoprotection with 30% sucrose in PBS (pH 7.4) for 24 h at 4°C. Tissue blocks containing the striatum were sectioned sagittally using a freezing microtome (SM2000R, Leica microsystems, Wetzlar, Germany) at 20 μm thickness. Floating sections were collected in 6 series and prepared for immunofluorescence to reveal the apposition between the PV neuron dendrites and corticostriatal or thalamostriatal terminals. For immunostaining, sections were incubated overnight at 4°C with a mixture of primary antibodies (Table 1) in incubation buffer containing 10% (v/v) normal donkey serum (Merck Millipore, Temecula, CA), 2% bovine serum albumin, and 0.5% (v/v) Triton X-100 in 0.05 M Tris-buffered saline (TBS, pH 7.4). After exposure to the primary antibodies, the sections were washed in PBS and incubated for 3 h at RT in the same incubation buffer containing a mixture of secondary antibodies that were conjugated to the fluorophores (Table 2). After rinsing, the sections were mounted onto glass slides and cover-slipped with ProLong Gold antifade reagent (Thermo Fisher Scientific).

Table 1. Primary antibodies used for research purposes

Antigen	Host Species	Clonality	Antigen	Dilution	Supplier	Catalog no.	RRID
GFP	Rat	mono	full length of His−GFP	1:5000	nacalai tesque	04404-26	AB_2313652
PSD95	Mouse	mono	aa77−299 of human PSD95	1:1000	NeuroMab	75-028	AB_2307331
PSD95	Rabbit	poly	aa68−251 of mouse PSD95	1:1000	Synaptic Systems	124 012	AB_2092359
PV	Guinea Pig	poly	full length of rat PV	1:5000	Synaptic Systems	195004	AB_2156476
PV	mouse	mono	frog PV	1:5000	Sigma Aldrich	P3088	AB_477329
VGluT1	Guinea Pig	poly	aa531−560 of mouse VGluT1	1:100	Frontier Institute	VGluT1-GP-Af570	AB_2571618
VGluT1	Guinea Pig	poly	aa552−560 of rat BNIP	1:100	Fujiyama et al., 2001	-	-
VGluT1	Rabbit	poly	aa531−560 of mouse VGluT1	1:100	Frontier Institute	VGluT1-Rb-Af500	AB_2571616
VGluT1	Rabbit	poly	aa554−582 of rat DNIP	1:100	Fujiyama et al., 2001	-	-
VGluT2	Guinea Pig	poly	aa559‑582 of mouse VGluT2	1:2000	Frontier Institute	VGluT2-GP-Af810	AB_2571621
VGluT2	Rabbit	poly	aa559‑582 of mouse VGluT2	1:2000	Frontier Institute	VGluT2-Rb-Af720 *	AB_2571619

*, the lot is currently not available. VGluT2-Rb-Af 860 (RRID: AB_2619683) is a current lot.

NeuroMab (Antibodies Inc., Davis, CA), Synaptic Systems (Goettingen, Germany), Sigma Aldrich (St. Louis, MO), Frontier Institute (Hokkaido, Japan).

Table 2. Secondary antibodies used in research

Secondary Antibody	Host Species	Dilution	Supplier	Catalog no.	RRID
Anti-Rat Alexa Fluor®488	Donkey	1:500	Thermo Fisher Scientific, Inc.	A21208	AB_141709
Anti-mouse Alexa Fluor®546	Donkey	1:500	Thermo Fisher Scientific, Inc.	A10036	AB_2534012
Anti-mouse Alexa Fluor®635	Goat	1:500	Thermo Fisher Scientific, Inc.	A31575	AB_2536185
Anti-Rabbit Alexa Fluor®405	Goat	1:500	Thermo Fisher Scientific, Inc.	A31556	AB_221605
Anti-Rabbit Alexa Fluor®635	Goat	1:500	Thermo Fisher Scientific, Inc.	A31577	AB_2536187
Anti-Guinea Pig Alexa Fluor®405	Goat	1:500	Abcam	ab175678	-
Anti-Guinea Pig Alexa Fluor®594	Goat	1:500	Thermo Fisher Scientific, Inc.	A11076	AB_141930
Anti-Guinea Pig Alexa Fluor®633	Goat	1:500	Thermo Fisher Scientific, Inc.	A21105	AB_2535757

All antibodies are polyclonal.

Thermo Fisher Scientific (Waltham, MA), Abcam (Cambridge, UK).

Fluorescent images were acquired using an inverted epifluorescence microscope (BZ-710, Keyence, Osaka, Japan) with a filter (excitation 470 ± 40 nm; emission 525 ± 50 nm) for GFP or AlexaFluor (AF) 488, and with a filter (excitation; 545 ± 25 nm; emission 605 ± 70 nm) for AF594. Afferent inputs onto the striatal GFP-positive dendrites were then observed under a confocal laser-scanning microscope (FV1200, Olympus, Tokyo, Japan) with appropriate lasers (405, 473, 559, and 635 nm) and filters (emission 430−455 nm for AF405, emission 490−590 nm for AF488 or GFP, emission 575−620 nm for tdTomato or AF546, emission 655−755 nm for AF633 or 635). Photos of tdTomato or AF546 and AF633 or AF635 were acquired using a high sensitivity detector (FV12-HSD, Olympus). Low-magnification images of AAV injection and axon terminal distribution were acquired using another epifluorescence microscope (BX-53, Olympus), with a U-FBNA filter (excitation 470−495 nm; emission 510−550 nm) for AF488 or GFP and with a U-FGWA filter (excitation 530−550 nm; emission 575−625 nm) for tdTomato.

For AAV injected mice, only sections of the ipsilateral hemisphere were analyzed and we selected sections containing a relatively high density of AAV labeled axon terminals in the dorsal striatum for the detailed analysis (Fig. 3E).

Putative axon terminals were identified as axonal varicosities (or swellings). We selected putative appositions where the putative axon terminals apposed with the membrane of a GFP-expressing dendrite or soma in three-dimensional views using confocal microscopy. In

our criteria for synaptic appositions, three components should be co-localized: a presynaptic terminal containing synaptic vesicles, a postsynaptic membrane, and a postsynaptic density. Therefore, we visualized these structures using multicolor immunofluorescence for post synaptic density protein 95 (PSD95) and VGluT1- and/or VGluT2-immunoreactivities in close apposition of AAV labeled axon terminals with PV dendrites (Fig. 5 and 6). In another experiment, we investigated all thalamostriatal and corticostriatal terminals using simultaneous immunostaining for both VGluT2 and VGluT1, respectively, without AAV labeling (Fig. 7 and 8).

Z-stack digital images were captured using a ×100 silicon oil immersion objective lens (Olympus) with the pinhole set at 230 μm. The images were deconvoluted using a free software Fiji (a distribution of Image J; Schindelin et al., 2012) and plugins (Diffraction PSF 3D and Iterative Deconvolve 3D; Dougherty, 2005). Point spread function (PSF) was calculated from the image of fluorophore beads of known diameter (TetraSpeck microspheres 0.5 μm, Invitrogen, Thermo Fisher Scientific). The z-axis shift caused by chromatic aberration was compensated by the Z-gap function of Fluoview (Olympus). To reconstruct dendritic trees of PV neurons, the z-stack images were imported to Neurolucida (MBF Bioscience, Inc., Williston, VT). Morphological parameters such as dendritic length and width in three-dimensional images and location of putative synaptic contacts were measured with NeuroExplorer (MBF). To calculate putative synapse density per unit length, the results

of "segment analysis" by NeuroExplorer were analyzed with a handmade function of MATLAB (MathWorks, Natick, MA).

2.3. In vitro electrophysiological recording and morphological observation of recorded neurons

To confirm that GFP was expressed in fast spiking PV-positive neurons in the striatum of PV-FGL mice (Kameda et al., 2012), in vitro whole-cell recording was conducted. One male mouse (P47 days) was anesthetized with sodium pentobarbital and perfused with 20-mL ice-cold modified ACSF (N-Methyl-D-glucamin 93; KCl 2.5; NaH_2PO_4 1.2; $NaHCO_3$ 30; HEPES 20; glucose 25; sodium ascorbate 5; thiourea 2; sodium pyruvate 3; $MgCl_2$ 10; $CaCl_2$ 0.5; in mM; pH adjusted to 7.3 by HCl). All ACSFs were aerated with 95%/5% O_2/CO_2 continuously. Then the brain was taken out and immersed in ice-cold modified ACSF for 2 min. Coronal slices of 300 μm thickness were cut using a vibratome (7000smz-2, Campden, Leicestershire, UK) and incubated with the modified ACSF at 32 °C for 15 min. The slices were transferred to the normal ACSF (NaCl 125; KCl, 2.5; $CaCl_2$, 2.4; $MgCl_2$, 1.2; $NaHCO_3$, 25; Glucose, 15; $NaHPO_4$, 1.25; pyruvic acid, 2; lactic acid, 4; in mM, pH 7.3) at RT. After 1 h of recovering, the slice was moved into a recording chamber (30 °C). A whole cell glass pipette (4‑6 MΩ) was filled with intracellular solution (K-methylsulfate 126; KCl 6; Na_2ATP 4; NaGTP 0.3; $MgCl_2$ 2; Na_4EGTA 0.6; HEPES 10; biocytin 20.1; in mM; pH adjusted to 7.3

16

by KOH and osmolality adjusted to ~290 mOsm). In the dorsolateral striatum, GFP expressing neurons were identified by a fluorescent microscopy (BX-51WI, Olympus) using a ×40 water-immersion objective lens (Fig. 2E1 and E2). Current clamp recordings were low-pass filtered at 10 kHz and recorded using EPC10 (HEKA Elektronik Dr. Schulze GmbH, Lambrecht/Pfalz, Germany) at a sampling rate of 20 kHz. The series resistance was examined by applying a brief voltage pulse (−5 or −10 mV for 10 ms) and was confirmed to be less than 20 MΩ. Shortly (less than 1 min) after the accomplishment of whole-cell configuration, the firing responses to 1-s of depolarizing current pulses (to 1000 pA by a 50 pA step) were recorded in current clamp mode. Then passive membrane properties were monitored by application of 1-s of hyperpolarizing current pulses (−20 to −100 pA by −20 pA steps or −50 to −200 pA by −50 pA steps). Since one of the main aims of the recording was to examine PV expression in the recorded neurons, the duration of recording was minimized (around 3–4 min) and the slice was kept in the perfused recording chamber for a few minutes after the electrode was withdrawn in order to wash out extracellularly leaked biocytin. Then the slice was fixed with 4% paraformaldehyde, 0.05% glutaraldehyde, and 0.2% picric acid in 0.1M PB overnight at 4°C, washed three times with (10 min per wash), and then re-sectioned at 50-μm thickness. These sections were incubated with 1% H_2O_2 in 0.05M TBS for 30 min at RT to deplete endogenous peroxidase, washed with TBS for three times, and incubated with a mouse antibody against PV (P3088, Sigma Aldrich; ×5000 diluted by the incubation buffer)

for overnight at 4°C. After washing three times in TBS, the sections were incubated with

streptavidin conjugated with CF350 (×1000; Biotium) and an anti-mouse secondary antibody

labeled with AF594 (×500; Thermo Fisher Scientific) for 3 h at RT. The sections were

observed with an epifluorescent microscope (BX-53). Finally, the sections were washed with

TBS and incubated with avidin-biotinylated peroxidase complex (ABC) solution (×200; Elite,

Vector) in TBS overnight at 4°C, and biocytin-filled neurons were visualized with Ni-DAB

using H_2O_2 (final concentration: 0.01%) under light microscopy. The sections were dried on a

slide glass and cover-slipped with EcoMount (Biocare Medical, LLC, Concord, CA).

2.4. Analysis of electrophysiological data

The analysis was performed by IgorPro (Wave Metrics Inc., Portland, OR) using the

Neuromatic plugin (http://www.neuromatic.thinkrandom.com). All recording data were

smoothed with a 0.2 ms moving time window corresponding to the moving average of 4

consecutive recording points. The input resistance (R_{in}) was determined by linear fitting of

voltage responses to hyperpolarized current pulses injection (−20 to −100 pA by −20 pA

steps). The membrane time constant (tau) was calculated from the response to a

−200-pA-current pulse by fitting the decaying phase with an exponential curve. Mean firing

frequency was calculated as the inverse of the mean interspike interval (ISI) during the first

200 ms of a depolarizing current pulse. The maximum firing frequency was calculated as the

inverse of the minimum ISI. To determine action potential threshold, membrane voltage

traces including the action potential elicited by the minimum intensity of a depolarizing pulse

were differentiated twice to obtain [(dV/dt)/dt]. The time point of the [(dV/dt)/dt] positive

peak just prior to the action potential peak was considered as the spike onset, and the

membrane potential at that time as the threshold. The full width of the spike was measured at

the threshold voltage. The amplitude of fast after-hyperpolarization (fAHP) was measured

from the threshold to the fAHP peak. fAHP delay was defined as the duration between the

peak of the action potential and the peak of the following AHP.

2.5. Statistical analysis

Data were provided as mean ± standard deviation (SD). Student's *t*-test was used to compare

the length (Fig. 4C) and diameter (Fig. 5C) of dendrites, and the apposition size (Fig. 5D).

Cumulative distribution of the dendritic diameter or the apposition size was compared using

the two-sample Kolmogorov-Smirnov test (Fig. 5C and 5D). The density of the appositions at

multiple locations along the dendrites was compared by one-way ANOVA followed by

post-hoc Tukey's multiple comparison tests (Fig. 6B, 6C, 7G and 8E). Analysis of covariance

(ANCOVA) was also performed to test whether the slopes were equal (Fig. 6C). Coefficient

of variation for the density of appositions on soma was defined as the ratio between the

standard deviation and the average value. Differences between groups were considered

statistically significant at $p < 0.05$. Apposition densities on somata were compared using the paired sample t-test (Fig. 8D). Statistical analyses were performed using R: a language and environment for statistical computing language (R Core Team, 2015). Curve fitting was performed by GraphPad Prism software (San Diego, CA). We analyzed and reported all apposition data in this study.

3. Result

3.1. Morphological features of parvalbumin (PV)-producing neurons in striatum

Parvalbumin-expressing neurons in PV-FGL transgenic mouse striatum were examined by detecting myrGFP-LDLRct with an anti-GFP antibody. GFP immunoreactivity was mostly observed well in the cell bodies and dendrites of the neurons throughout the striatum (arrowheads in Fig. 2A). To verify the specificity of GFP expression in PV neurons, brain sections of PV-FGL mice were immunostained for PV and the numbers of PV-expressing and GFP-expressing neurons were counted in the whole striatum (LM 2.52–3.25 mm). The vast majority of GFP-immunoreactive neuronal cell bodies also exhibited PV immunofluorescence (93.3% ± 0.3%, N = 331 cells from 3 sections in 3 mice). Likewise, the vast majority of PV-immunoreactive neuronal cell bodies (95.5% ± 3.3%, N = 323 cells from 3 sections in 3 mice) exhibited GFP immunofluorescence (Fig. 2C). The GFP neurons were also distributed homogeneously in the striatum in 3 sagittal sections of the striatum (lateromedial (LM) 1.2, 1.8 and 2.4 mm, Fig. 2D; cf. Kita et al., 1990). The expression profiles were consistent with previous reports of PV expression in rodent brains (DeFelipe, 1993; Hontanilla et al., 1997; Klausberger and Somogyi, 2008; Miyamoto and Fukuda, 2015; Wheeler et al., 2015). These results indicate that GFP expression is specific to PV-expressing neurons in the PV-FGL mice. Within a single PV cell, GFP immunoreactivity was distributed along the whole dendritic membrane of the dendritic shaft, which was optically sectioned by

confocal laser scanning microscopy (Fig. 2B1 green).

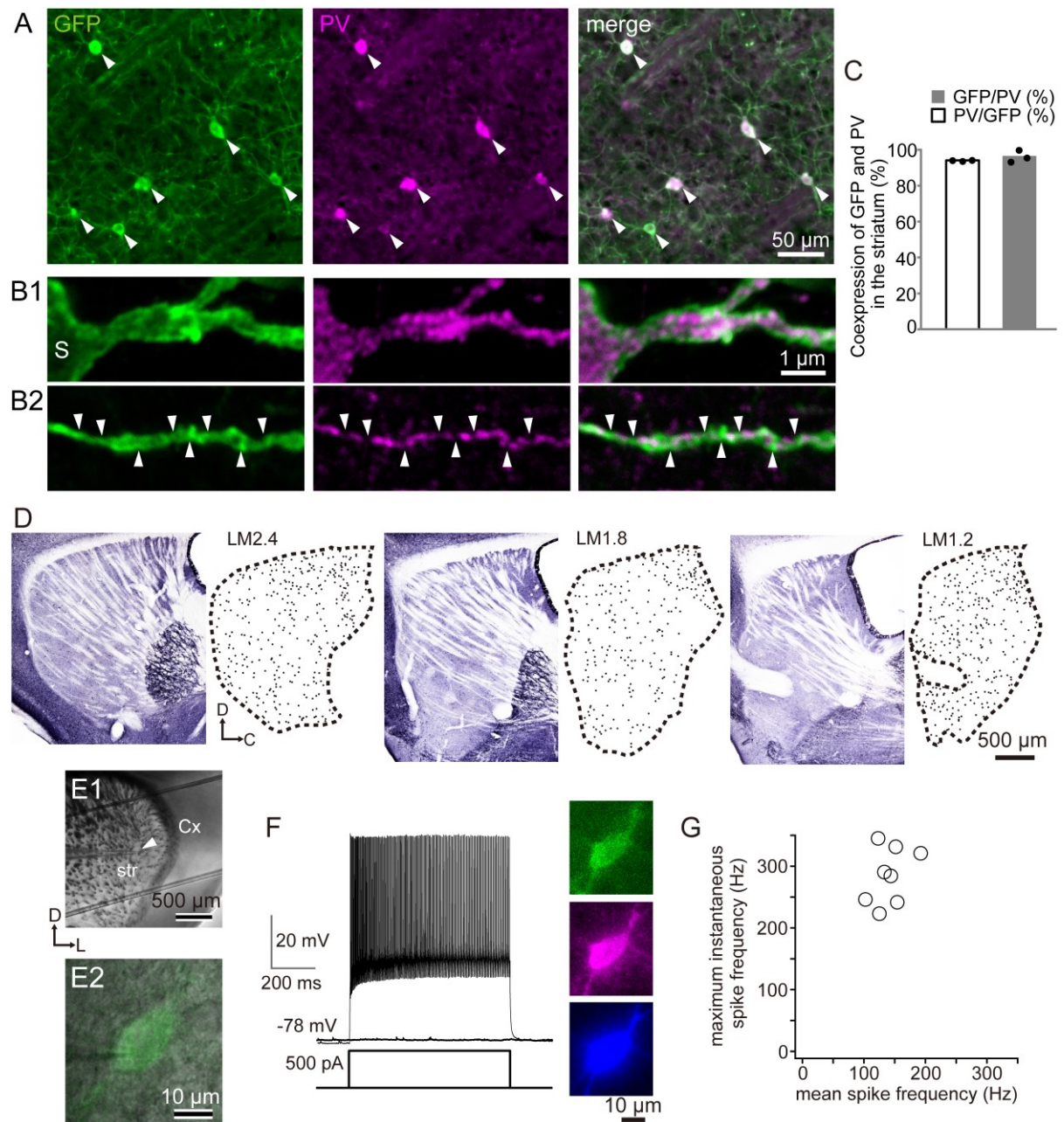**Fig. 2:** Morphological and electrophysiological characterizations of GFP expressing parvalbumin (PV) neurons in the striatum. **A, B**. Double immunofluorescence labeling for GFP and PV in the striatum of PV-FGL mice. Low- (A) and high-magnification (B) images showing GFP (AF488) and PV (AF594) double immunofluorescence labeling in the striatum. Note that most of GFP immunopositive neurons

22

showed PV immunoreactivity (arrowheads in A). Plasma membrane of the dendrites of striatal neurons was more clearly labeled with GFP rather than PV immunoreactivity (B1, S represents the soma), especially in thin dendrites. Arrowheads in B2 indicate portions of the dendrite visualized with dense GFP but very weak PV immunofluorescence. Photos were acquired with an inverted epifluorescence microscope (BZ-710, Keyence, Osaka, Japan) (A) and with a confocal laser-scanning microscope (FV1200, Olympus, Tokyo, Japan) (B) under the conditions described in the Materials and Methods. **C.** Proportions of GFP neurons co-expressing PV (open bar, N = 331 cells from 3 sections in 3 mice; shown as dots) and proportions of PV neurons co-expressing GFP (filled bar, N = 323 cells) in the striatum. **D**. Distribution of GFP immunoreactivity in the striatum of PV-FGL transgenic mice. GFP neurons were scattered throughout the striatum in different lateromedial subdivisions (LM 1.2, 1.8 and 2.4 mm) of the striatum (drawn from one mouse). Photos were acquired with a microscope (BX-53, Olympus, Tokyo, Japan) in brightfield. **E-G**. Electrophysiological and morphological confirmation of GFP expressing neurons in the striatum of PV-FGL mice. E. An example of whole cell recorded neurons. E1, a coronal slice containing the dorsolateral striatum, where GFP expressing neurons were recorded using a patch electrode (arrowhead). E2, a merged image of a recorded neuron in a living slice by IR-DIC (in grayscale) and fluorescent (green) conditions. Cx, cortex; str, striatum. F. Left, an example of a depolarized current pulse induced non-accommodated and high frequency firing in a GFP expressing neuron. Right, an example of immunostaining of the recorded neuron filled with biocytin. GFP (top), PV-immunofluorescence (middle), and biocytin (bottom). PV was detected in all GFP neurons examined (N = 6/6). G. Maximum

23

instantaneous firing frequency was plotted against mean spike frequency during a 200 ms depolarizing

current pulse (N = 8 cells from one mouse). See also Table 3.

In contrast, intense PV immunofluorescence was observed only at the middle of the dendritic

shaft, reflecting the lack of association with the membrane (Fig. 2B1 magenta). Moreover,

unlike GFP fluorescence, PV fluorescence was discontinuous across thin dendrites

(arrowheads in Fig. 2B2), indicating that FGL is more suitable for dendritic labeling and

evaluation of synaptic distribution than PV immunoreactivity.

3.2. Electrophysiological and morphological properties of GFP expressing striatal neurons in PV-FGL mice

To confirm GFP expression in PV-positive fast spiking interneurons, we recorded from GFP

expressing neurons in the dorsolateral striatum of PV-FGL mouse using in vitro slice

preparation (Fig. 2E1, E2; note that the in vitro slices were coronally sectioned), where

motor-related cortical and thalamic axons densely projected (see Fig. 3). Their firing

properties were investigated using depolarizing current pulses, and the recorded neurons

demonstrated fast-spiking activity with little frequency adaptation (Fig. 2F the left column

and Fig. 2G; N = 8 cells). The mean firing frequency was 140.75 ± 26.79 Hz (range 102.6‑

192.19 Hz) during the first 200 ms of a 1s depolarizing-pulse. The maximum instantaneous

firing frequency was 285.44 ± 45.18 Hz (range 223.19‑345.23 Hz; Fig. 2G). These

characteristic fast spikes were comparable with those reported earlier on striatal PV neurons

(Kawaguchi et al., 1995; Gittis et al., 2010; Gittis et al., 2011; Straub et al., 2016). Further, hyperpolarized resting membrane potential, narrow spike width, fast after hyperpolarization with large amplitude, low input resistance, and short membrane time
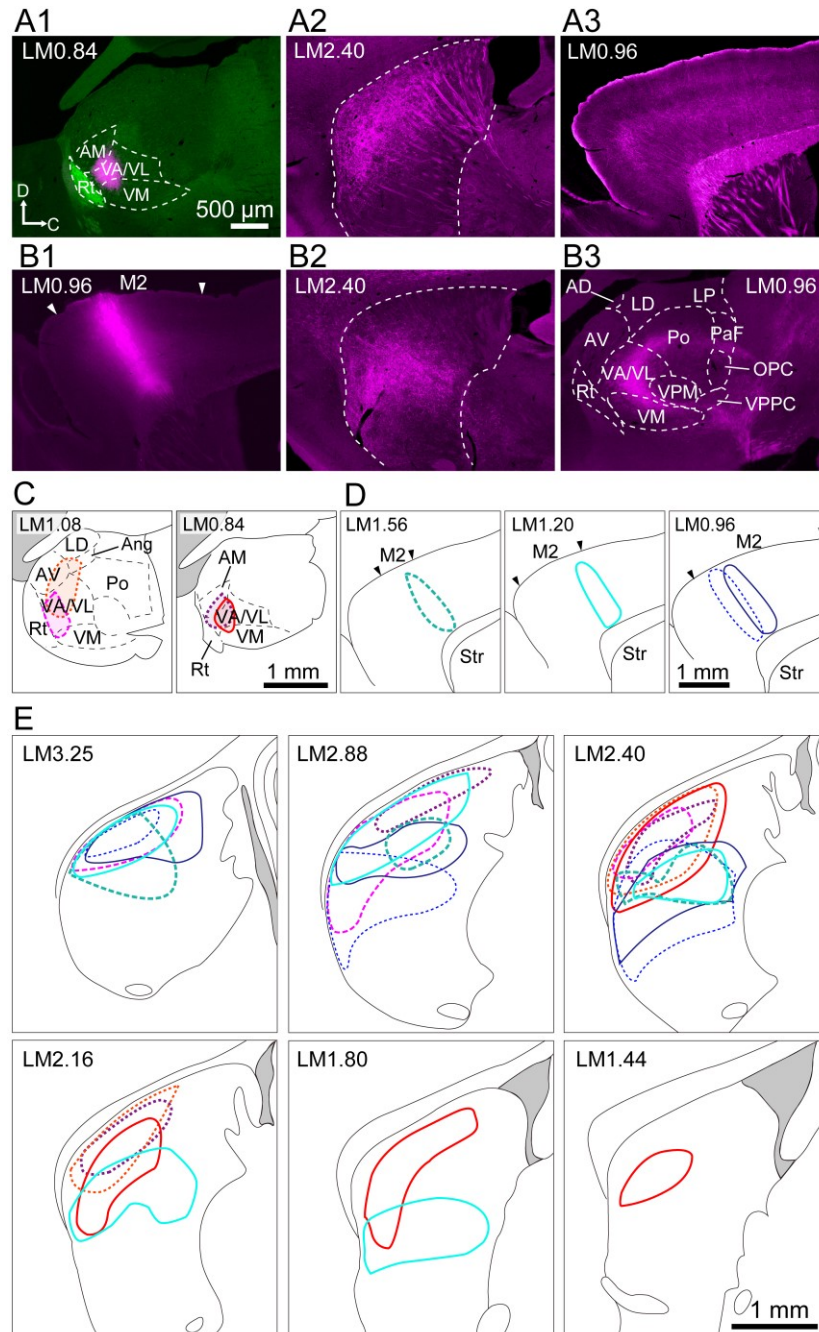

Fig. 3: Distributions of axon collaterals from the motor-related cerebral cortex and thalamus. **A, B**.

Low-magnification images showing the viral injection site in the ventral thalamus (A1) and M2 (B1).

Subnuclei of the thalamus were identified with GFP immunoreactivity (A1). VA/VL is located on the

caudal side of Rt immunoreactive for GFP. Fluorescent images of axons of thalamostriatal and

corticostriatal terminations following tracer injections of AAV in the ventral thalamus and M2 are shown in

A2 and B2, respectively. AAV labeled axons originating from VA/VL were also distributed in the frontal

cortex, especially in layer I, III and V (A3). AAV labeled axons originating from M2 were also distributed

in the thalamus, including VA/VL (B3). Photos were acquired with an epifluorescent microscope (BX-53,

Olympus, Tokyo, Japan) under the conditions described in the Materials and Methods section. AD,

anterodorsal thalamic nucleus; AM, anteromedial thalamic nucleus; Ang, angular thalamic nucleus; AV,

anteroventral thalamic nucleus; LD, laterodorsal thalamic nucleus; LP, lateralposterior thalamic nucleus;

OPC, oval paracentral thalamic nucleus; PaF, parafascicular thalamic nucleus; PC, paracentral thalamic

nucleus; Po, posterior thalamic nuclear group; Rt, reticular nucleus (prethalamus); VA/VL, ventral anterior

/ ventral lateral complex; VM, ventromedial thalamic nucleus VPM, ventral posteromedial thalamic

nucleus; VPPC, ventral posterior nucleus of the thalalamus parvicellular. The boundaries of thalamic

nuclei were drawn in reference to the mouse brain atlas (Paxinos and Franklin, 2013). **C, D**. The location

and areal extent of tracer injections of AAV in the ventral thalamus (C) and M2 (D) are illustrated with solid

and dotted lines in different lateromedial subdivisions (LM 0.84−1.56 mm). For each injection case,

different colors of lines and shades are used. The red color group is for thalamic injections and blue color

group for cortical injections. For the verification of injection site of four cases each, see supplementary

figure 1. **E**. Topography of corticostriatal and thalamostriatal terminations following injections is also

illustrated in the same planes in different lateromedial subdivisions (LM 1.44−3.25 mm). Color code is the

same as in C and D.

constant were also consistent with the previous reports (Table 3; cf. Kawaguchi, 1993; Gittis

et al., 2010). Finally, triple fluorescent staining for GFP, PV, and biocytin confirmed that

these neurons co-expressed PV (Fig. 2F the right column; N = 6/6). By preliminary

observation, it was not clear whether GFP was expressed toward the very ends of dendrites.

To confirm, we first observed GFP expression by immunohistochemistry with Ni-DAB

visualization; however, in the striatum, GFP was expressed not only in dendrites but also in

axons. The dense axon collaterals prevented the tracing of thin dendrites until their

terminations. Therefore, single GFP neurons were labeled by biocytin using a patch pipette.

Comparison between biocytin labeling and GFP expression revealed that GFP was indeed

expressed even in far and thin dendrites.

3.3. Projection of axon fibers from motor-related cortex and thalamus

The injection site of AAVdj-CAG-hChR2-H134R-tdTomato was confirmed by fluorescent

microscopy. For example, in Figure 3A1, tdTomato fluorescence was restricted mainly to

the rostral part of the thalamic VA/VL. Thalamic nuclei were approximately identified

using the patterns of autofluorescence and GFP expression because GFP expressing

neurons were also densely distributed in the thalamic reticular nucleus (Rt). In addition to thalamus, AAV was injected into the M2 area of motor cortex (Fig. 3B1). In preliminary experiments, we confirmed that immunofluorescence for Neurofilament 200 kD (N200; Sigma Aldrich N0142) was useful for distinguishing M2 from M1 (Ueta et al., 2013), and the corresponding coordinates were used for AAV injections. Due to the limitation in the number of fluorescent colors, we did not directly examine N200 immunofluorescence for the injections shown in Figure 3. The locations of all injection sites in the VA/VL (N = 4 mice) or M2 (N = 4 mice) were traced onto the sagittal planes in Figures 3C and D, respectively (see also supplementary fig. 1).

The populations of AAV-labeled axons after injection into VA/VL or M2 were not distributed uniformly but exhibited a clear topographical organization in the ipsilateral dorsal striatum at around LM 2.40 mm (Fig. 3A2, B2 and E). It is also notable that the labeled axons originating from VA/VL were widely distributed in the frontal cortex, especially in layers I, III, and V (Fig. 3A3), whereas the axons originating from M2 were widely distributed in the thalamus, including VA/VL (Fig. 3B3).

We found common features of motor-related corticothalamic and thalamostriatal axon distribution in relation to the LM axis of the striatum. In the lateral striatum (LM 2.16 – 3.25 mm), both corticothalamic and thalamostriatal axons were oriented toward the dorsolateral striatum (Fig. 3E). The results of the present study support convergent striatal projections

from ventral thalamic and frontal cortical motor areas as described previously by retrograde tracing (McFarland and Haber, 2000).

3.4. AAV-labeled cortical and thalamic inputs to PV-producing interneurons

To examine the distribution of corticostriatal and thalamostriatal terminals on PV-dendrites, we traced a PV dendrites from their somal origins to endings (due to branching, one primary dendrite has multiple endings). Only when a given ending was authentic (naturally ended within section) the dendritic path from the origin to the ending of the dendrite was examined for the following analysis (Fig. 4B). We did not obtain apposition data from dendritic paths whose distal tips were cut by brain sectioning. According to this criterion, we obtained 30 dendritic trees with 42 authentic ends derived from 22 PV neurons for the analysis of thalamostriatal appositions (N = 2 mice). Also, corticostriatal appositions were analyzed on 30 dendritic trees with 53 authentic ends from 25 PV neurons (N = 3 mice). Due to the limitation of multicolor imaging, samples for corticostriatal or thalamostriatal terminals were derived from different mice. The location of all sample dendrites fell within the area of labeled VA/VL or M2 axons (Fig. 3E, 4A). No significant differences were observed in the average dendritic length (distance from soma to the authentic ending) among the samples examined for the AAV-labeled thalamic or cortical appositions (Fig. 4C, thalamostriatal: 110.9 ± 25.2 μm, N = 42, corticostriatal: 100.0 ± 32.5 μm, N = 53, $p = 0.08$ by two-sided t-test). Therefore, dendrite

selection was designed to minimize sampling bias by including approximately equal lengths of

dendrites.

Table 3. Electrophysiological properties of GFP expressing striatal neurons

	Mean ± SD	Range
Resting membrane potential (mV)	−79.79 ± 4.11	−73.1 − −86.29
Spike width (ms)	0.77 ± 0.08	0.61 − 0.88
Input resistance (MΩ)	53.90 ± 11.20	44.21 − 72.45
Time constant (ms)	1.78 ± 1.00	0.83 − 3.75
fAHP amplitude (mV)	18.90 ± 3.33	15.18 − 24.82
fAHP delay (ms)	1.29 ± 1.23	0.6 − 3.85

Data were derived from 8 neurons.

fAHP: fast after-hyperpolarization
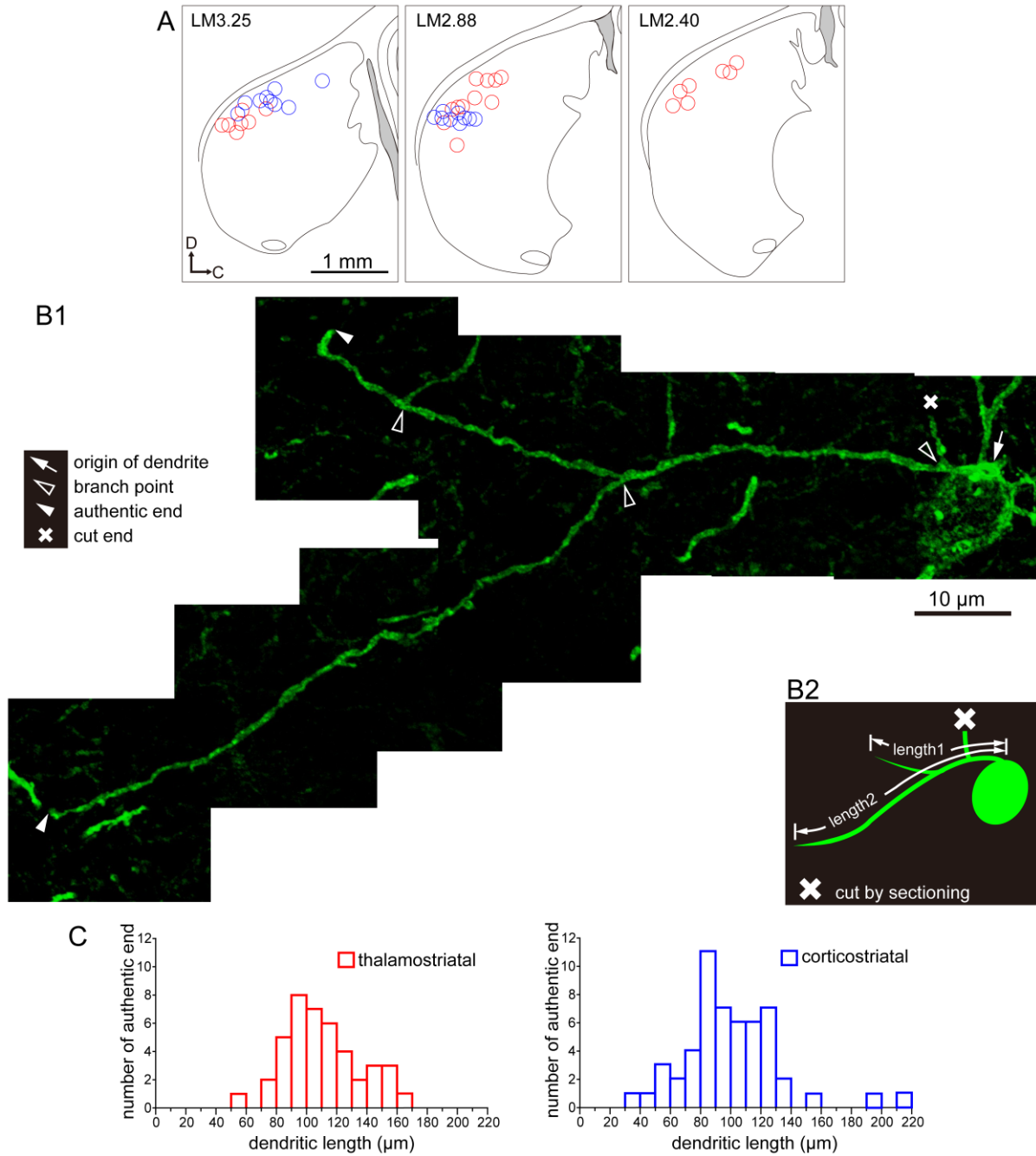
Fig. 4: Sampling method for thalamostriatal and corticostriatal appositions. **A**. The locations of PV neurons analyzed in the present study. Red and blue circles indicate PV neurons analyzed for thalamostriatal and corticostriatal appositions, respectively. The locations of PV neurons from all mice are projected onto the single nearest lateromedial planes (LM 2.40, 2.88, 3.25 mm). Note that the location of all sample dendrites falls within the area of AAV labeled axons after injection into VA/VL or M2 shown in

Figure 3E. Thalamostriatal: N = 25 cells in 2 mice, corticostriatal: N = 22 cells in 3 mice. **B**. A reconstructed dendritic tree of a PV-producing striatal interneuron. The dendrites with authentic endings (an actual distal tip ending within a section, filled arrowheads) continuous with the dendritic origin are included for the analysis. In contrast, the dendrites separated by brain sectioning (×) are considered as artificial cut ends and are excluded from the analysis. The length is measured from the origin of dendrite (arrow) to the respective authentic ends for each examined dendrite as shown in B2 (length 1 and 2). Photos were acquired with a confocal laser-scanning microscope (FV1200, Olympus, Tokyo, Japan) at every 0.48 μm of depth from top to bottom of the dendrite. **C**. Histograms showing frequencies of the dendritic lengths (with authentic endings only) of the PV neurons used for the observation of thalamostriatal (red) and corticostriatal (blue) inputs. Thalamostriatal: 110.9 ± 25.2 μm, N = 42 lengths derived from 30 dendritic trees of 25 cells in 2 mice, corticostriatal: 100.0 ± 32.5 μm, N = 53 lengths derived from 30 dendritic trees of 22 cells in 3 mice. $p = 0.08$ by two-sided t-test.

To confirm the synaptic nature of the PV-positive peridendritic structures, triple staining was performed for GFP, either VGluT1 (marker of cortical projections) or VGluT2 (marker of thalamic projections), and the excitatory postsynaptic marker, postsynaptic density protein 95 (PSD95) (Fig. 5A, B). Presynaptic terminals putatively forming synapses with the dendritic shafts of PV neurons were identified in the images of VGluT1 or VGluT2 immunoreactivity.
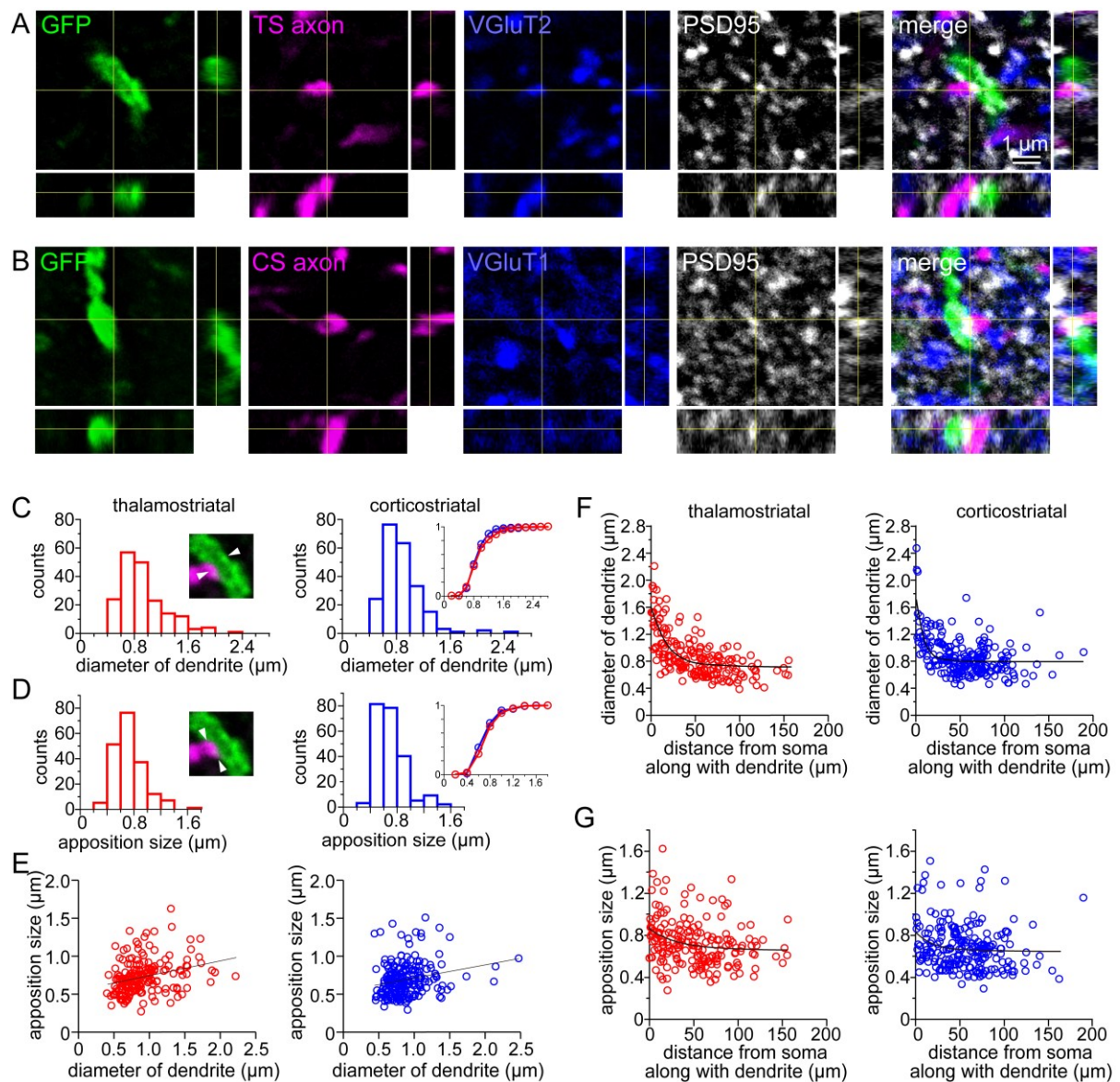
Fig. 5: Quantitative analysis of apposition density on PV dendrites by thalamic or a cortical axon terminals.

A, **B**. A dendritic apposition on PV neurons by thalamic (A) or cortical (B) axon terminals associated with PSD95. Quadruple fluorescence images of PV dendrites (green), AAV-labeled axon structures (magenta), VGluTs (blue), and PSD95 (gray) in the striatum. AAV-labeled axon terminals with VGluT1 or VGluT2 immunoreactivity formed close appositions on PV dendrites. PSD95 stainings are closely located to these structures. Note that the PV dendrite surface, PSD95 immunoreactivity, either VGluT1 or VGluT2 immunoreactivity, and AAV-labeled terminals are co-localized in a single confocal plane; orthogonal views are also presented at the thin yellow line plane. Merged views are shown in the right-most column. Photos were taken with a confocal laser-scanning microscope (FV1200, Olympus, Tokyo, Japan) at every

34

0.1 μm of depth to capture entire dendrite under the conditions described in the Materials and Methods. **C**. Frequency distribution of postsynaptic dendrite diameter for each apposition. Diameter was measured as shown in the image (straight length between arrowheads) for the thalamostriatal (red, N = 189 appositions; 30 dendrites of 25 PV neurons from 2 mice) and the corticostriatal terminals (blue, N = 218 appositions; 30 dendrites of 22 PV neurons from 3 mice). There is no significant difference in mean diameter between dendrites receiving thalamostriatal or corticostriatal inputs ($p = 0.20$ by t-test; 0.91 ± 0.34 μm for thalamostriatal and 0.87 ± 0.29 μm for corticostriatal samples). For comparison, the cumulative curves are shown in the inset. No difference is detected by Kolmogorov-Smirnov test ($p = 0.54$). **D**. Frequency distribution of apposition size measured as shown in the image (straight length between arrowheads). The mean of thalamostriatal and corticostriatal apposition sizes are 0.73 ± 0.22 μm (N = 189) and 0.69 ± 0.22 μm (N = 218), respectively. The difference is not significant ($p = 0.06$). Cumulative curves are shown in the inset. Again, the difference is not significant ($p = 0.11$). **E**. Relationship between the apposition size and dendrite diameter. Note the significant linear correlation (thalamostriatal: $R^2 = 0.087$, $p < 0.0001$, N = 189; corticostriatal: $R^2 = 0.052$, $p = 0.0007$, N = 218). **F**. Relationship between dendrite diameter and distance from the parent soma. Black lines indicate fitted exponentials and show decreasing diameter with distance (thalamostriatal, $R^2 = 0.530$, decay constant = 17.95 μm, corticostriatal, $R^2 = 0.391$, decay constant = 8.45 μm). **G**. Relationship between the apposition size and the distance from the soma. Black lines indicate fitted exponential decreases of the apposition size with distance (thalamostriatal, $R^2 = 0.070$, decay constant = 31.15 μm, corticostriatal, $R^2 = 0.043$, decay constant = 23.46 μm).

As shown in Figures 5A and B, quadruple immunofluorescence images indicated that AAV-labeled axon terminals with immunoreactivity for either VGluT were in close apposition with PSD95 on PV dendrites. Since the PSD95 serves as a cytoskeletal anchor in excitatory synapses and provides a scaffold for other postsynaptic proteins, excitatory

synapses were probably observed in such appositions. In the present study, AAV-labeled axon terminals with VGluT1 or VGluT2 immunoreactivity that contacted PSD95-immunoreactive puncta on PV dendrites were considered as synaptic appositions. In total, 189 such synaptic appositions were observed for thalamostriatal and 218 for corticostriatal axons. We then examined the morphological properties of postsynaptic dendrites for all synaptic appositions. There was a little tendency that mean diameter of the dendrites apposed by the thalamostriatal terminals was larger than the ones apposed by the corticostriatal terminals (Fig. 5C, thalamostriatal: 0.91 ± 0.34 μm, N = 189, corticostriatal: 0.87 ± 0.29 μm, N = 218), but the difference was not significant ($p = 0.20$ by t-test). Cumulative distributions were also similar (Fig. 5C right inset, $p = 0.54$ by two-sample Kolmogorov-Smirnov test). For the apposition size, there is a tendency that the thalamostriatal appositions were larger than the corticostriatal ones (Fig. 5D, thalamostriatal: 0.73 ± 0.22 μm, N = 189, corticostriatal: 0.69 ± 0.22 μm, N = 218), although the difference did not reach statistical significance ($p = 0.06$ by t-test). Similarly, cumulative distributions did not differ (Fig. 5D, right inset, $p = 0.11$ by two-sample Kolmogorov-Smirnov test). In both populations, apposition size and the diameter of the postsynaptic dendrite were positively correlated (Fig. 5E; thalamostriatal: $R^2 = 0.087$, $p < 0.0001$; corticostriatal: $R^2 = 0.052$, $p = 0.0007$). Also, the decrease in dendritic diameter along the dendritic length fit a single exponential decay model for both populations (Fig. 5F, black lines indicate the fitted

exponential; thalamostriatal: $R^2 = 0.530$, decay constant = 17.95 µm, corticostriatal: $R^2 = 0.391$, decay constant = 8.45 µm).

We also investigated the relationship between the size of appositions and the distance from the soma. The plots could be fitted with a single exponential decay curve (Fig. 5G, black lines indicate the fitted exponential; thalamostriatal: $R^2 = 0.070$, decay constant = 31.15 µm, corticostriatal: $R^2 = 0.043$, decay constant = 23.46 µm) indicating that appositions decrease in size with dendritic distance from the soma.

The number of thalamostriatal appositions appeared greater along proximal dendrites than distal dendrites (Fig. 6A). However, the number of sampled dendrites was not equal among bins defined by distance from the soma due to dendritic branching. Therefore, the density of appositions was calculated for individual dendrites by dividing the number of appositions by the total length of dendrites included in each 10 µm bin. Although the SD was relatively large, the mean apposition density decreased gradually with distance for thalamostriatal appositions (red line in Fig. 6B left) and the linear correlation was significant ($R^2 = 0.034$, N = 189, $p = 0.0004$). However, our samples contained relatively few appositions far from the soma (Fig. 6A1, A2), as reflected by the large SDs within each bin, especially for short dendrites. For example, if a given bin contained only two dendrites, and one dendrite is 1 µm-long and has one apposition, the density is 1.0, while if another is 9.5 µm long with one apposition, the density is 0.11, yielding a SD of 0.63. This kind of large variance should mask a real

37
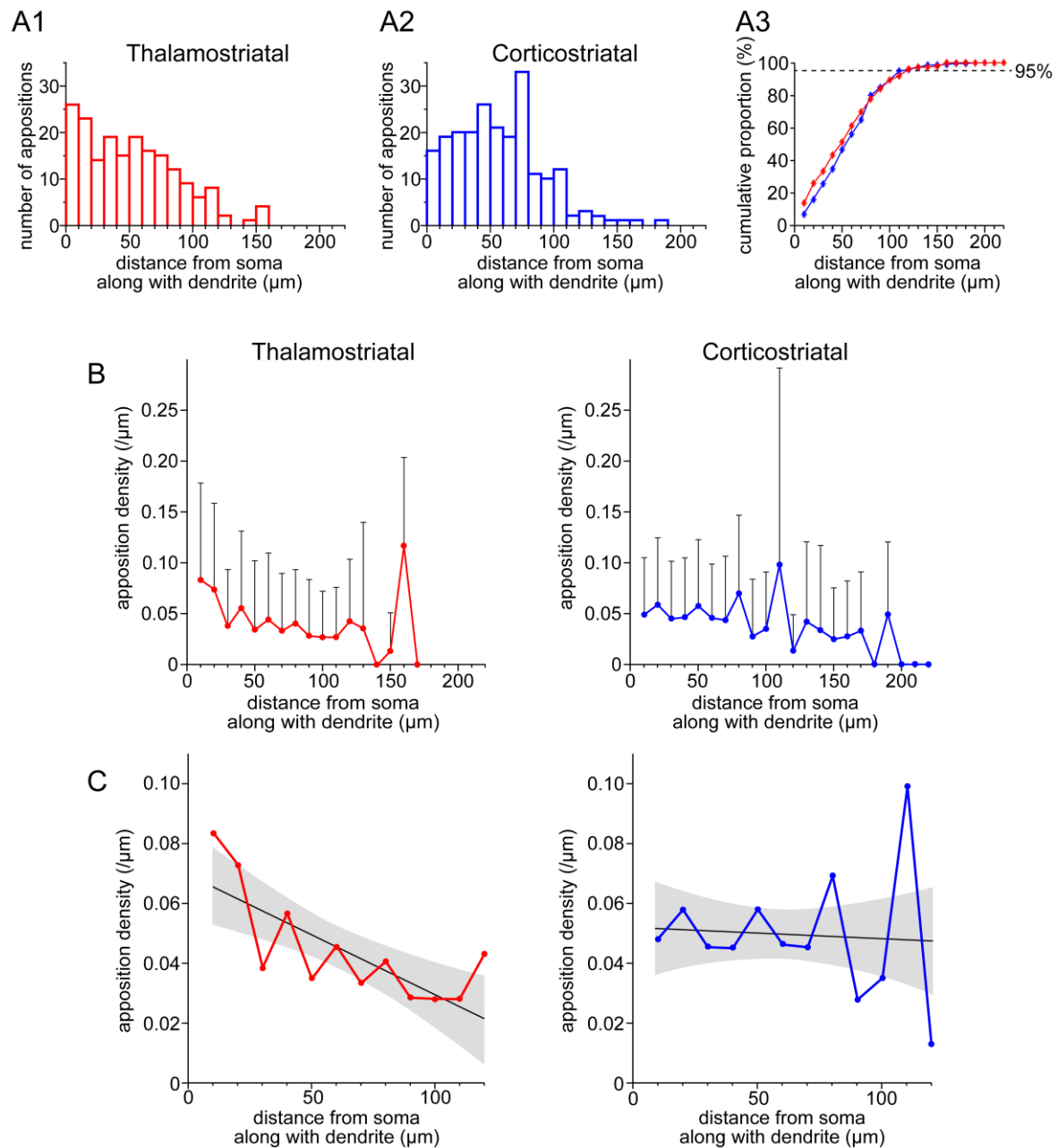
Fig. 6: Statistical analysis of dendritic appositions on PV neurons by cortical or thalamic axon terminals.

A1, **A2**. Frequency distribution of the number of appositions against dendritic distance from somata along

with the dendrites examined for the thalamostriatal (red; N = 189 appositions from 2 mice) and

corticostriatal inputs (blue; N = 218 appositions from 3 mice). **A3**. Cumulative proportion of the apposition

numbers revealed that more than 95% of appositions were obtained closer than 120 μm from the parent

soma for both thalamostriatal (red) and corticostriatal inputs (blue). Two-sample Kolmogorov-Smirnov

test showed that there was no significant difference in the cumulative proportion between inputs (A3, $p = 0.08$). **B**. The mean apposition frequencies per total length of dendrites within each 10-μm bin (apposition density) with distance from the soma for thalamostriatal (red) and corticostriatal (blue) inputs. The mean density of thalamostriatal appositions is significantly higher over the proximal 20-μm of dendrite than over the distal portion (Tukey's multiple comparison test after one-way ANOVA; $p < 0.05$ for the density in 0−20 μm *vs.* other locations. See text for details). In regression analysis, the slope of the linear fitting is significantly different from zero ($R^2 = 0.034$, $p = 0.0004$, N = 189 for thalamostriatal appositions). In contrast, no significant difference in the density of corticostriatal appositions (blue) was noticed between the proximal and distal portions of the dendrite (one-way ANOVA; $p = 0.39$). Regression analysis revealed no significant correlation between apposition density and distance from the soma ($R^2 = 0.006$, $p = 0.15$, N = 218 for corticostriatal appositions). **C**. Regression analysis of densities in the thalamostriatal (red) and corticostriatal (blue) appositions within 120 μm of the soma. Black lines and the shaded bands indicate the regression lines and 95% confidence intervals, respectively. In regression analysis, the slope of the linear regression line is significantly different from zero ($R^2 = 0.040$, $p = 0.0002$, N = 182 for thalamostriatal appositions). In contrast, the slope of linear regression line for corticostriatal appositions did not differ from zero ($R^2 = 0.0002$, $p = 0.78$, N = 209).

relationship between the apposition density and distance from the soma. Since over 95% of the appositions were within 120 μm from the soma (the dotted line in Fig. 6A3 shows 95% of

cumulative proportion), we excluded the data beyond 120 μm. The mean and 95%

confidence intervals of linear fittings for the densities were plotted against the distance from

the soma (Fig. 6C). The mean curve could be linearly fitted (the black line in Fig. 6C). The

slope of the linear fit differed significantly from a flat line (slope = 0), indicating a negative

correlation (Fig 6C left; $R^2 = 0.040$, $p = 0.0002$, N = 182). In addition, the slopes of the linear

fit of thalamostriatal and corticostriatal inputs were significantly different (Fig 6C, $p = 0.03$).

Moreover, when the densities were combined in 20-μm bins (0−20, 20−40, 40−60, 60−80,

80−100, and 100−120 μm groups), one-way ANOVA followed by post-hoc Tukey tests

revealed that apposition density of thalamostriatal projections was significantly higher within

20 μm of the cell body than at other locations ($p = 0.0004$ by ANOVA; $p = 0.014$ *vs.* 40−60

μm, $p = 0.006$ *vs.* 60−80 μm, $p = 0.0005$ *vs.* 80−100 μm, and $p = 0.010$ *vs.* 100−120 μm by

Tukey test). Among other locations, no significant difference was observed ($p = 0.86$−0.999).

In contrast, when corticostriatal appositions were analyzed in the same way (the right panels

in Fig. 6B and 6C), no significant change in the density of corticostriatal appositions was

found with distance. In other words, corticostriatal appositions were uniformly distributed on

PV dendrites (in Fig. 6B right, $R^2 = 0.006$ $p = 0.15$, N = 218; in Fig. 6C right, $R^2 = 0.0002$, p

$= 0.78$, N = 209).

3.5. VGluTs immunolabeled terminals on the dendrite of PV neurons

For quantitative analysis of all the corticostriatal and thalamostriatal appositions on PV neurons, not only from motor-related areas, triple immunofluorescence staining for VGluT1, VGluT2, and PSD95 was performed (Fig. 7C-E and 8A-C). Only VGluT1- or VGluT2-immunoreactive axon terminals contacting PSD95-immunoreactive sites on PV dendrites were analyzed. The locations of all sample PV neurons (N = 12 cells in 2 mice) are shown in Figure 7A, and these samples fell within the area where the analysis of motor-related terminals was carried out (see, Fig. 3E). Fifteen PV dendrites derived from 12 neurons were sampled approximately 20, 60, 80, 100 and 140 μm away from the cell body along dendritic branches (Fig. 7B). The mean length of sampled dendrite was 23.87 ± 3.80 μm (range: 12.28–31.90 μm; N = 39 segments), and for each segment, the number of VGluT1-positive or VGluT2-positive terminals apposed onto the dendrite was counted. The counting was performed within the range less than 5 μm from the section surface because VGluT1 immunoreactivity was drastically attenuated with depth. In total, 528 VGluT2-positive appositions and 1160 VGluT1-positive appositions were identified (Fig. 7D and E). Representative data obtained from 8 of the 15 dendrites examined are shown in Figure 7F, in which ≥ 3 dendritic locations were sampled from single dendrites (N = 394 for VGluT2-positive appositions and N = 889 for VGluT1-positive appositions). Accordingly, the density of VGluT2-positive appositions gradually decreased along with the distance from the soma in accord with results for VA/VL axon terminals, whereas the density of

41

VGluT1-positive appositions did not change with distance. All data, also containing dendrites in which <3 locations were investigated, are plotted in Figure 7G. The density of VGluT2-positive appositions was almost 10 times larger than that determined by AAV labeling of VA/VL axons. The relationship between the VGluT2-positive apposition density and distance could be linearly fitted (not shown in Fig. 7G left, R^2 = 0.473, N = 528 appositions), and the slope was significantly different from zero (p < 0.0001). Mean VGluT2 density also decreased along with distance (red curve). The apposition densities at each dendritic location were compared by one-way ANOVA and post-hoc Tukey's multiple comparison tests. We found that the apposition density at 20 μm away from the soma was significantly larger than at other distances (p < 0.05; Fig. 7G left). Beyond 60 μm, the densities did not differ significantly. In contrast, we observed neither significant correlation between the density of VGluT1-positive terminals and distance (Fig. 7G right, R^2 = 0.005, p = 0.68, N = 1160 appositions), nor significant differences of the densities at each location (p = 0.80, by one-way ANOVA). Therefore, the terminals from the motor-related cortex (Fig. 6C) and all VGluT1-positive terminals (Fig. 7G) were uniformly distributed along PV dendrites.

3.6. VGluTs immunolabeled terminals on the soma of PV neurons

For examination of axosomatic appositions, a region of interest (ROI) was sampled for each soma by selecting a part of the somatic membrane from which no dendrite or axon issued

(Fig. 8A-C). The thickness of the ROIs was ~3 μm in the z dimension, corresponding to ~15 confocal planes. The perimeter length of sampled somatic membrane ranged from 13.84 to 37.91 μm (21.64 ± 6.92 μm for 10 PV somata). The mean apposition density of VGluT2 immunoreactive terminals was 0.58 ± 0.22 per μm (N = 124 appositions from 10 PV somata in 2 mice) and that of VGluT1-immunoreactive terminals was 0.92 ± 0.07 per μm (N = 199 appositions). Similar with the dendrites, the density of VGluT1-positive appositions was

A

LM3.25   LM2.88   LM2.40

D
└→C   1 mm

B

C

20μm   60μm   100μm

10 μm

E   D

5 μm

D

GFP   VGluT2   VGluT1   PSD95   merge

E

1 μm

F

VGluT2

VGluT1

apposition density (/μm)

distance from soma
along with dendrite (μm)

G

apposition density (/μm)

***
***
*
**

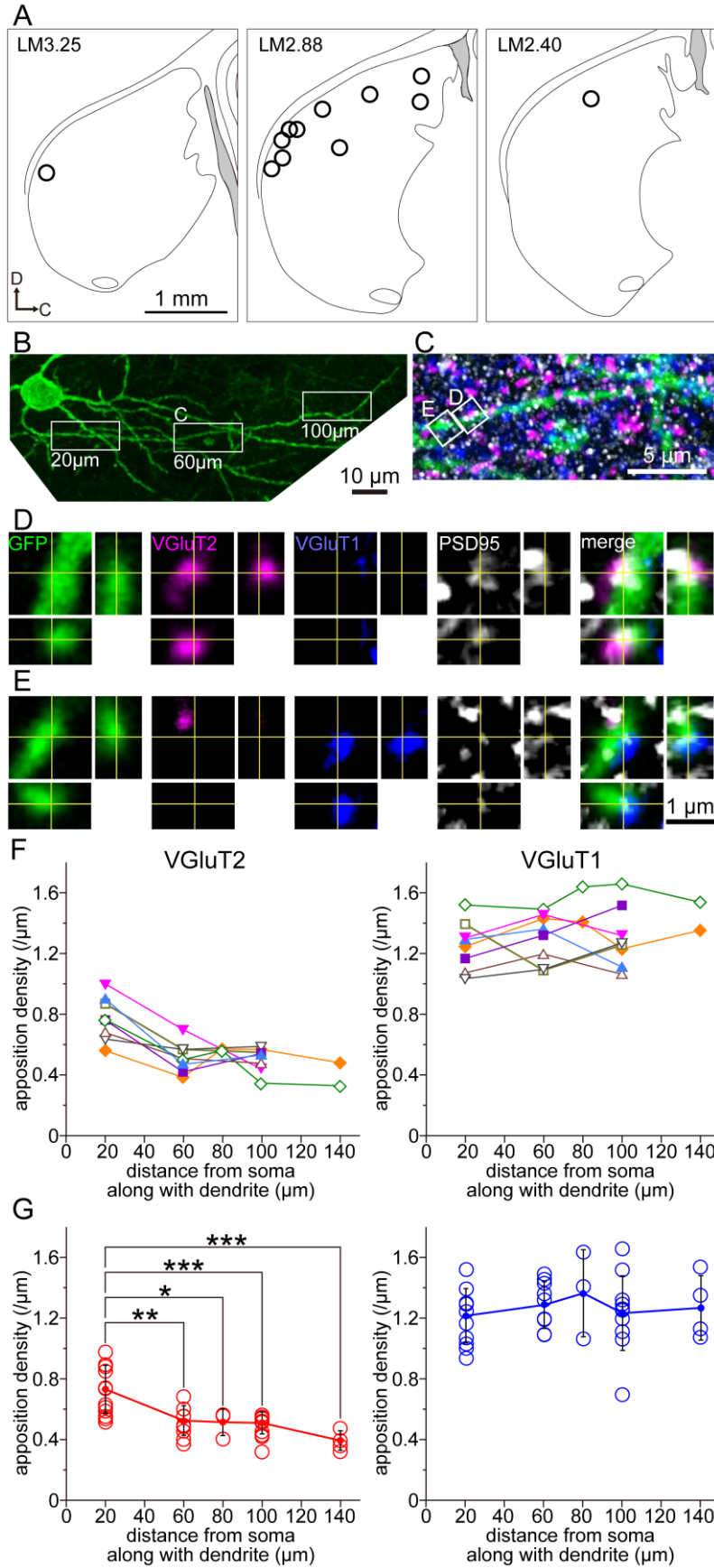distance from soma
along with dendrite (μm)

Fig. 7: Quantitative analysis of dendritic appositions on PV neurons by VGluT2 or VGluT1 immunoreactive terminals. **A**. The location of twelve PV neurons for the quantitative analysis of entire cortico- and thalamo-striatal appositions. All PV neurons fell within the areas of VA/VL and M2 axon distributions (see, Figure 3E). **B**. A low-magnification maximum intensity projection image shows a PV neuron. A dendrite issuing form the bottom of the soma was analyzed. Three boxes represent a region of interest (ROI) investigated for apposition density. Mean distance from the soma to ROIs are also indicated. **C**. High-magnification image showing quadruple immunofluorescence of GFP, VGluT2, VGluT1 and PSD95 at the PV dendrite from the boxed area shown in B. **D, E**. Higher-magnification images showing quadruple immunofluorescence of GFP, VGluT2, VGluT1 and PSD95 at the PV dendrite from the boxed areas shown in C. Note that the PV dendrite surface, PSD95, and either VGluT1 or VGluT2 immunoreactive axon varicosities were co-localized in a single confocal plane; orthogonal views are also presented at the thin yellow line plane. Merged views are shown in the right most column. Photos were acquired with a confocal laser-scanning microscope (FV1200, Olympus, Tokyo, Japan) at every 0.2 μm of section depth as to capture the entire dendrite under the conditions described in the Materials and Methods. **F**. The apposition densities of the VGluT2 (left; N = 394 appositions) and VGluT1 (right; N = 889 appositions) immunoreactive terminals against the distance from the somata along the dendrites. The number of ROIs is 8 at 20 μm; 8 at 60 μm; 2 at 80 μm; 8 at 100 μm; and 2 at 140 μm from somata. More than 3 different locations were investigated in these 8 dendrites. **G**. The mean apposition densities of VGluT2 (left, red) and VGluT1 (right, blue) immunoreactive appositions on 15 PV dendrites against the distance from 20, 60, 80, 100 and 140 μm somata alongside the dendrites. The number of ROIs is 12 at 20

µm; 9 at 60 µm; 3 at 80 µm; 11 at 100 µm; and 4 at 140 µm from somata. Note that the number of VGluT2-positive (thalamostriatal) appositions per dendritic length was significantly higher on the proximal portion than on the distal portion of the dendrites (*, $p < 0.05$; **, $p < 0.01$; ***, $p < 0.001$ by Tukey's multiple comparison test after one-way ANOVA. N = 528 appositions on 15 dendrites from 12 cells in 2 mice). There is no significant difference in the densities of VGluT1-positive (corticostriatal) appositions between the proximal and distal portions of the dendrites ($p = 0.68$, N = 1160 appositions).

higher than that of VGluT2 ones in all ROIs (Fig. 8D; $p = 0.0016$ by the paired t-test). The ratio of VGluT2- to VGluT1-immunoreactive appositions at the soma (shown at zero of the horizontal axis in Fig. 8E), and at each dendritic location was compared by one-way ANOVA followed by post-hoc Tukey's multiple comparison test (Fig. 8E). We found that the ratio of VGluT2- to VGluT1-immunoreactive appositions was significantly higher on the proximal portion of the cell, including the soma, than on distal dendrites (*, $p < 0.05$, Fig. 8E).
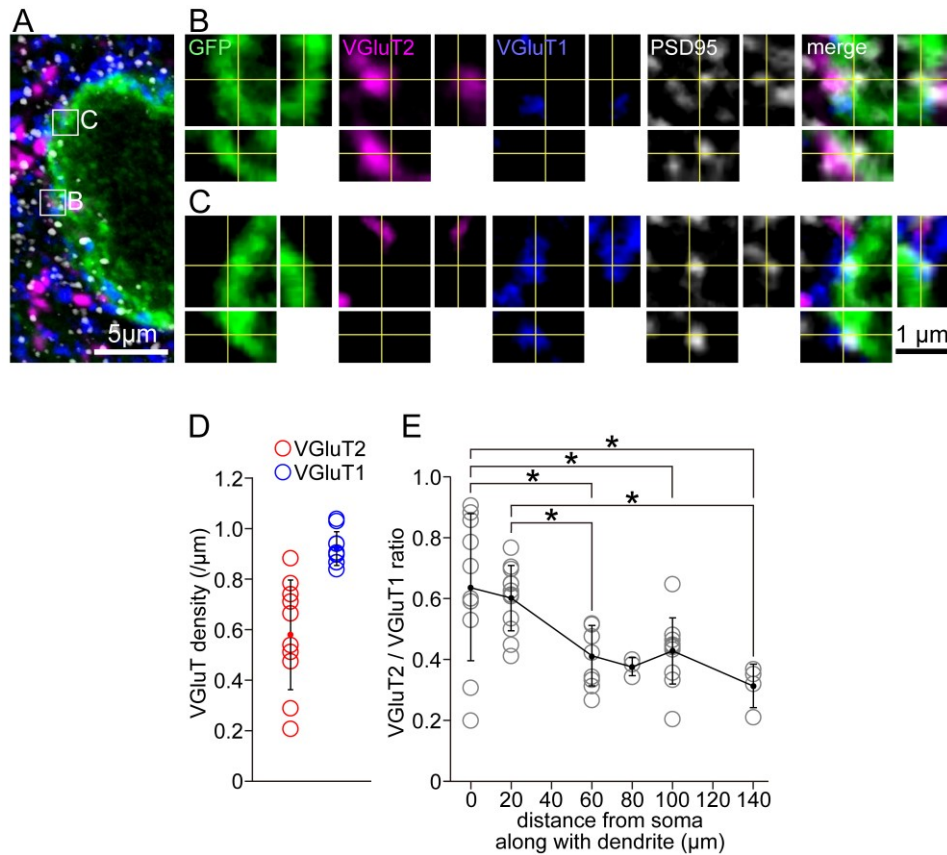
Fig. 8: Quantitative analysis of somatic appositions on PV neurons by VGluT2- or VGluT1-immunoreactive axon terminals. **A**. A low-magnification image showing quadruple immunofluorescence of GFP, VGluT2, VGluT1, and PSD95 at the PV soma. For this PV neuron, 25.39 μm of membrane (in perimeter) was investigated for apposition density. **B, C**. High-magnification images showing quadruple immunofluorescence of GFP, VGluT2, VGluT1 and PSD95 at the PV soma from the boxed areas shown in A. Note that GFP, PSD95, and either VGluT1 or VGluT2 immunoreactivities were co-localized in a single confocal plane; orthogonal views are also presented at the thin yellow line plane. Merged views are shown in the right-most column. Photos were taken with a confocal laser-scanning microscope (FV1200, Olympus, Tokyo, Japan) at every 0.2 μm of depth to capture the soma under the conditions described in the Materials and Methods. **D**. The apposition densities on 10 PV somata for the VGluT2-immunoreactive

47

(red circles) and VGluT1-immunoreactive (blue circles) terminals. VGluT1-positive terminals were more densely distributed than VGluT2-positive ones (**, $p < 0.01$). **E**. The ratio of VGluT2- to VGluT1-immunoreactive appositions on 10 PV somata. Note that the ratio of VGluT2- to VGluT1-immunoreactive appositions was significantly higher on the proximal portion of the dendrites and soma than on the distal portion of the dendrites (*, $p < 0.05$ by Tukey's multiple comparison test after one-way ANOVA. N = 10 somata from in 2 mice).

4. Discussion

In the present study, we first showed that glutamatergic inputs originating from VA/VL motor thalamus preferentially contact the proximal dendrites of PV neurons as measured by apposition number per unit length, while inputs from motor cortex exhibit no such dendritic location preference (Fig. 6). We obtained similar results by measuring the numbers of terminals expressing VGluT2 or VGluT1 (Fig. 7). The advantage of the former measurements is that it reduces uncertainty due to heterogeneity of presynaptic neurons, whereas the advantage of the latter is that it measures a larger number synapses, including those from non-motor areas. Thus, the proximal preference of thalamostriatal synapses on PV neurons is likely shared by other thalamic nuclei (Fig. 9).

4.1. Technical considerations

In the present study, VGluT1 and VGluT2 immunoreactivities were used as markers of cortical and thalamic excitatory terminals, respectively. However, some studies reported that VGluT1 mRNA has been detected in some thalamic neurons (Fremeau et al., 2004; Barroso-Chinea et al., 2007), suggesting that VGluT2 immunoreactivity might not be an exclusive marker for thalamic terminals. Conversely, when thalamic neurons in the ventrobasal thalamic nuclei were chemically ablated, most of the VGluT2 immunoreactivity

Cortex including M2

Dorsolateral striatum

PV

Thalamus including VA/VL
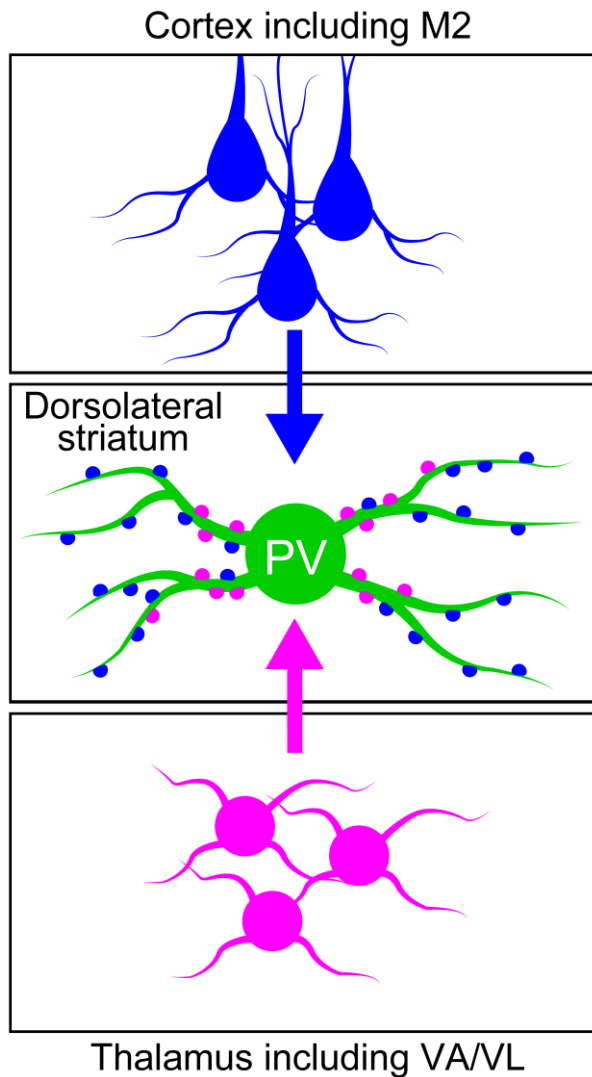
fig. 9: The density of thalamostriatal appositions (red) along the dendritic length was higher on the proximal portion than on the distal portion of the striatal parvalbumin (PV) dendrites (green). In contrast, no significant difference in the frequency of the appositions with the cortical terminals (blue) was noticed between the proximal and distal portions of the dendrite.

disappeared from the primary sensory cortex, while VGluT1 immunoreactivity did not change significantly (Fujiyama et al., 2001). Moreover, in the cerebral cortex, mRNA is weakly expressed only in layer 4 (Hisano et al., 2000); however, layer 4 neurons never project to subcortical regions such as the striatum (Lorente de Nó, 1992). In the present study, over 87% of all anterogradely labeled VA/VL and M2 axonal boutons apposing PV dendrites within 5 μm of the section surface were VGluT2-immunoreactive and

VGluT1-immunoreactive, respectively. In addition, these terminals always apposed with PSD95-immunoreactive puncta on PV dendrites. Therefore, VGluT1 and VGluT2 immunoreactivities in the present study can be used as nearly selective, if not exclusive, markers for cortical and thalamic excitatory axon terminals, respectively. Another technical consideration is that variations in the location of AAV injection and infection efficiency may have affected our results; however, we observed very similar location patterns for thalamostriatal and corticostriatal terminals on PV dendrites using VGluTs immunoreactivity or AAV labeling (cf. Fig. 6 and 7).

4.2. Comparison of corticostriatal and thalamostriatal inputs among striatal neuron types

As concerned with the cortical inputs, previous ultrastructural studies combined with anterograde tracing have revealed that corticostriatal afferents primarily formed synapses with dendritic spines in the striatum of cat (Kemp and Powell, 1971; Frotscher et al., 1981), monkey (Smith et al., 1994), and rat (Hattori et al., 1979; Somogyi et al., 1981; Dubé et al., 1988; Xu et al., 1989; Wictorin et al., 1989; Wilson et al., 1990; Hersch et al., 1995). In those studies, the postsynaptic neurons were predominantly MSNs because dendrites of most other striatal interneurons are aspiny. By combining morphological analyses with VGluT1 immunoreactivity, we and others found that more than 80% of VGluT1-immunopositive

terminals (likely of cortical origin) form axospinous synapses rather than direct axodendritic synapses in the striatum (Fujiyama et al., 2006; Raju et al., 2006; Lacey et al., 2005; Lei et al., 2013). Nevertheless, taken together with the fact that > 85% of striatal neurons are MSNs the high proportion of axospinous synapses (80%) in VGluT1-positive synapses could occur just by chance without special preference for MSNs to other interneurons. Conversely, a considerable number of contralaterally projecting corticostriatal terminals have been reported to form the synapse with dendritic shafts in cat (Kemp and Powell, 1971) and rat (Hersch et al., 1995). Therefore, VGluT1-positive appositions in the present study (Fig. 7 and 8) should include a sizable proportion of these contralaterally projecting terminals, whereas AAV-labeled terminals were only from the ipsilateral hemisphere.

As for the thalamic terminals, previous studies of synaptic organization using VGluT2 immunoreactivity have found that thalamic terminals are more often on dendritic shafts than are cortical terminals, although there is considerable study-to-study variation in frequency (Fujiyama et al., 2006; Raju et al., 2006; Lacey et al., 2005; Lacey et al., 2007; Lei et al., 2013). Therefore, it is possible that thalamic terminals are preferentially located on aspiny interneurons, including PV neurons, compared to cortical terminals. However, it is still unclear whether thalamostriatal terminals preferentially target striatal interneurons, and if so which population.

For cell type preference of thalamostriatal and corticostriatal appositions we could compare

two data sets. Huerta-Ocampo et al. (2014) reported densities of 0.577 VGluT1-positive

terminals per μm and 0.286 VGluT2-positive terminals per μm on MSN dendrites by electron

microscopy (EM) (recalculated from their data to get the average for D1- and D2-MSNs). In

the current study, total apposition densities on PV neurons were 1.246 per μm for VGluT1-

and 0.567 per μm for VGluT2-positive terminals by confocal microscopy, almost double

those for MSNs. However, the experimental methods were different, so this cell type

dependence must be re-evaluated more carefully to conclude.

With regard to preferential targeting by corticostriatal *versus* thalamostriatal terminals, the

ratio of VGluT1-positive/VGluT2-positive terminal density was 2.02 for MSNs (calculated

from Huerta-Ocampo et al., 2014) and 2.20 for PV neurons (1160 VGluT1-positive and 528

VGluT2-positive terminals in 930.92 μm of PV neuron dendrites). Therefore, it is probable

that both MSNs and PV neurons receive almost double the number of corticostriatal inputs

versus thalamostriatal inputs despite huge differences in neuronal density. Alternatively,

other striatal cell types may show distinct distribution patterns. Previous studies showed that

cortical and thalamic afferents project complementary inputs to specific subclasses of striatal

interneurons. Cholinergic interneurons are known to receive more robust glutamatergic input

of thalamic origin than cortical origin (Lapper and Bolam, 1992; Ding et al., 2010). In

contrast, neuropeptide Y (NPY)/SOM neurons receive inputs from the cortex but not the

thalamus, whereas neurogliaform neurons expressing NPY (NPY/NGF neurons) are innervated by both pathways (Vuillet et al., 1989; Kachidian et al., 1996; Assous et al., 2017).

4.3. The motor thalamus, as one of the sources of thalamostriatal projections

Thalamostriatal projections were massively derived from the intralaminar nuclei (IL) and midline nuclei, and from the ventral thalamic nuclei (Veening et al., 1980; Parent and De Bellefeuille, 1983; Hazlett and Bagley, 1983; Beckstead, 1984; Takada et al., 1985a; Takada et al., 1985b; Berendse and Groenewegen, 1990; Lapper and Bolam, 1992; Sidibe and Smith, 1999; Erro et al., 2001; Smith et al., 2004; Bayer and Glimcher, 2005; Raju et al., 2006; Barroso-Chinea et al., 2007; Ellender et al., 2013). Although it is known that the afferents from IL onto PV neurons are sparse in comparison to cortical afferents (Rudkin and Sadikot, 1999), optogenetic stimulation of axon terminals originated from large area of thalamus elicits PV excitation (Sciamanna et al., 2015). This suggests that thalamic nuclei other than the IL, including ventral nuclei, are also likely to innervate the striatum. The single neuron tracing studies revealed that the axon collaterals originating from motor thalamus, both IZ of VA-VL complex and VM motor nuclei project to the striatum (Kuramoto et al., 2009; Kuramoto et al., 2015) but there are few reports on the properties of those synapses on striatal PV neurons from motor thalamus. Since the PV neurons are known to receive cortical inputs

from the motor cortex in rat (Bennett and Bolam, 1994; Ramanathan et al., 2002) and monkey (Lapper et al., 1992), they may integrate the motor information from motor related cortical and thalamic neurons and provide inhibition onto MSNs (Gittis et al., 2010). Indeed, our present result revealed that VA/VL terminals formed appositions on striatal PV neurons. They occupied at least approximately 10% of all thalamostriatal terminals (cf. Fig. 6C and 7G), although precise estimation is impossible because the number of VA/VL neurons infected by AAV is unknown.

As mentioned above, there is substantial study-to-study variation in the frequency of the axospinous contact for the thalamostriatal terminals (Fujiyama et al., 2006; Raju et al., 2006; Lacey et al., 2005; Lacey et al., 2007; Lei et al., 2013). The study-to-study variation is thought to depend on whether striosome or matrix are examined (Fujiyama et al., 2006; Raju et al., 2006) and on the difference in thalamic origin. Many studies have revealed that the individual thalamic nuclei differ in their preferential target dendrites or spines. The caudal IL has been shown to make synaptic contacts primarily with dendritic shafts in rat (Dubé et al., 1988; Xu et al., 1991; 2005; Lacey et al., 2007) and monkey (Sadikot et al., 1992; Smith et al., 1994). Indeed, Raju et al. (2006) reported that 89% of intrastriatal terminals from the parafascicular nucleus end on dendrites in rats. In contrast, some rostral IL nuclei sent thalamostriatal axons that made contacts mainly with dendritic spines (Xu et al., 1991; Ichinohe et al., 2001). An electrophysiological experiment also verified the heterogeneity of

thalamostriatal inputs from IL (Ellender et al., 2013). We could not examine such variability among VA/VL neurons here because the injection sites were generally restricted to the anterior part of VA/VL (Fig. 3C), corresponding to IZ in the rat. Although the posterior part of VA/VL, corresponding to EZ, does not project to the striatum (Kuramoto et al., 2009), we still cannot exclude the possibility of heterogeneity among VA/VL neuron targets.

4.4. Physiological and morphological differences between corticostriatal and thalamostriatal synapses and their functional implications

A recent combined optogenetic and electrophysiological study reported that corticostriatal and thalamostriatal synapses on PV neurons showed postsynaptic facilitation and postsynaptic depression, respectively (Sciamanna et al., 2015). In addition to an increased release probability and quantal EPSC size, thalamostriatal synapses exhibited more prominent AMPA-mediated currents than corticostriatal synapses (Sciamanna et al., 2015). Although the mean size of appositions was not significantly different between corticostriatal and thalamostriatal terminals in the present study, there was a tendency for larger thalamostriatal terminals were large (p = 0.06; Fujiyama et al., 2006; but see also Liu et al., 2011; Lei et al., 2013). In addition, a significant correlation was observed between apposition size and diameter of the postsynaptic dendrites (Fig. 5E). The amplitude of synaptic potential is proportional to the product of synapse number (or number of release sites), release

probability, and quantal size (for review, Stevens, 2003). Collectively, the dependence of release probability on synaptic junctional size (Holderith et al., 2012) and the number of postsynaptic receptors (Nusser et al., 1997; Tanaka et al., 2005), the correlation of quantal amplitude and synapse size (Mackenzie et al., 1999), and the proximal location preference of thalamostriatal terminals may contribute to reliable synaptic transmission from thalamostriatal terminals. Assuming that the dendrites of PV neurons are electrophysiologically passive at least below the threshold (Norenberg et al., 2010; Kameda et al., 2012), the positional preference of thalamostriatal terminals to proximal PV dendrites would produce large electric driving forth with less attenuation, allowing thalamostriatal inputs to act as drivers (Shermann and Guillery, 1998; Lee and Sherman, 2010). In contrast, concurrent population or repetitive activities would be required for cortical inputs to affect striatal PV neurons strongly due to their weak individual strengths (Kincaid et al., 1998; Stern et al., 1998; Wilson and Groves, 1981; Wilson, 1992). Moreover, considering their smaller size and distal location, cortical inputs more likely act as modulators of the local balance between dendritic excitation and inhibition. In addition, the mean interbouton interval was ~10 μm for corticostriatal axons (Kincaid et al., 1998) and ~9 μm for VA/VL cells in the IZ zone (calculated from Table 2 in Kuramoto et al., 2009). Therefore, it is likely that the chance of synapse formation onto PV neurons is similar for individual corticostriatal and thalamostriatal neurons. Thus, a larger number of corticostriatal neurons converge onto

single PV neurons than thalamostriatal neurons given that apposition density was two-times larger for corticostriatal terminals. It could also imply the modulatory role for corticostriatal terminals. However, it should be noted that if striatal PV neurons shared the cable properties of PV-positive basket cells in the hippocampus, distal inputs would be amplified (Norenberg et al., 2010). Further studies are required to uncover physiological differences in synaptic properties and efficacies dependent on synaptic locations.

PV neurons are considered the main source of inhibition to MSNs (Koos and Tepper, 1999; Tepper et al., 2004; Gustafson et al., 2006; Mallet et al., 2006; Planert et al., 2010; Gittis et al., 2010; Sciamanna et al., 2015). In addition, it has been reported that the corticostriatal and thalamostriatal synapses on MSNs showed postsynaptic facilitation and postsynaptic depression, respectively (Ding et al., 2008), as similar to other cortical or thalamic terminals (Lindström and Wróbel, 1990; Lee and Sherman, 2008; Timofeev and Steriade, 1997; Turner and Salt, 1998; von Krosigk et al., 1999). Therefore, PV neurons are thought to produce powerful feedforward inhibition on MSNs in response to thalamic and/or cortical inputs. This inhibition may play a role in tuning the timing of MSNs firing precisely. The reason of small difference between thalamostriatal and corticostriatal apposition size in the present study could be partially ascribed to that previous researches usually included the medium spiny neuron, of which the size of every axospinous contact are limited by the post spine size. This limit would affect the data of synaptic size unevenly on the basis of the preference of

thalamostriatal or corticostriatal projection.For further understanding of thalamostriatal and corticostriatal inputs onto the striatal neurons, the following four points must be considered. First, the precise source of cortical inputs should be identified because it is well known that corticostriatal inputs are derived from two distinct pyramidal cell types: pyramidal tract type and intratelencephalon type or crossed corticostriatal neurons (Wilson, 1987). The striatal axons of the former type are collaterals of deep subcortical projections toward pontine nuclei and/or spinal cord, while axons of the latter innervate only the cortex and striatum in both hemispheres. These two types of pyramidal neurons are known to differ in multiple respects (Reiner et al., 2003, 2010; Lei et al., 2004; Chen et al., 2005; Morishima and Kawaguchi, 2006; Molyneaux et al., 2007; for review see Shepherd, 2013). Therefore, it is possible they also differentially innervate PV neurons, although these inputs had similar electrophysiological effects on MSNs (Kress et al., 2013). It is also important to compare ipsilateral and contralateral innervation patterns. Second, recent reports have documented considerable heterogeneity even among striatal PV neurons (Garas et al., 2016; Kosaka et al., 2017). A subpopulation of PV neurons preferentially target indirect pathway MSNs in rat (Garas et al., 2016). In contrast, Gittis et al. (2010) found that Lxh6 expressing fast spiking interneurons preferentially project direct pathway MSNs in mice. PV neurons involved in distinct pathways may also differ in excitatory input properties. Manchado et al. (2016) reported that 20% of ionotropic serotonin receptor subunit 3a (5HT3a) expressing

interneurons co-expressed PV. In addition, there is an evidence that 41% of striatal Lhx6 expressing neurons show fast spiking physiological property, indicating that they are PV interneurons (Gittis et al., 2010). These reports indicate that PV neurons are constituted by some subgroups. In the present study, the coefficient of variation (CV) of somatic input density from thalamus and cortex to striatal PV neurons exhibited considerable difference (0.35 in thalamostriatal, 0.07 in corticostriatal) (Fig. 8D). The greater CV of thalamostriatal input probably occurred from small number of thalamic inputs or the heterogeneity of PV neurons. Third, while we focused on cortical inputs from M2 in this study; however, the striatum receives a wide range of inputs from multiple cortical areas. The M2 area is activated earlier than M1 or striatum during action selection tasks in rats (Sul et al., 2011) and is often considered as the counterpart of higher order motor-related area of the primates, although the function of rodent M2 is still in debated (Saiki et al., 2014). Corticostriatal projections could also differ among cortical areas, and M1 inputs must be further examined for distribution and synaptic properties. Fourth, recent research has revealed another type of striatal interneurons (NPY/NGF) that also provides massive inhibition onto MSNs via $GABA_B$ receptors (Ibanez-Sandoval et al., 2011; English et al., 2012). These interneurons may also function as integrators of corticostriatal and thalamostriatal inputs to control MSNs activities. The above consideration may also help explain some variation within our data (for example large SDs shown in Fig. 6). Altogether, further detailed investigation of such

heterogeneous inputs onto different PV neuron subpopulations (and onto other interneurons)

is required to elucidate the functional differences between corticostriatal and thalamostriatal

innervation.

5. Reference

Alexander, G.E., and Crutcher, M.D. (1990). Functional architecture of basal ganglia circuits: neural substrates of parallel processing. *Trends. Neurosci.* 13, 266–271.

Alexander, G.E., DeLong, M.R., Strick, P.L. (1986). Parallel organization of functionally segregated circuits linking basal ganglia and cortex. *Annu. Rev. Neurosci.* 9, 357–381.

Assous, M., Kaminer, J., Shah, F., Garg, A., Koós, T., Tepper, J.M. (2017). Differential processing of thalamic information via distinct striatal interneuron circuits. *Nat. Commun.* 8, 15860.

Barroso-Chinea, P., Castle, M., Aymerich, M.S., Perez-Manso, M., Erro, E., Tunon, T., Lanciego, J.L. (2007). Expression of the mRNAs encoding for the vesicular glutamate transporters 1 and 2 in the rat thalamus. *J. Comp. Neurol.* 501, 703–715.

Bayer, H.M., and Glimcher, P.W. (2005). Midbrain dopamine neurons encode a quantitative reward prediction error signal. *Neuron.* 47,129–141.

Beckstead, R.M. (1984). A projection to the striatum from the medial subdivision of the posterior group of the thalamus in the cat. *Brain Res.* 300, 351–356.

Bennett, B.D., and Bolam, J.P. (1993). Characterization of calretinin-immunoreactive structures in the striatum of the rat. *Brain Res*. 609, 137–148.

Bennett, B.D., and Bolam, J.P. (1994). Synaptic input and output of parvalbumin-immunoreactive neurons in the neostriatum of the rat. *Neuroscience*. 62, 707–719.

Bentivoglio, M., Balercia, G., Kruger, L. (1991). The specificity of the nonspecific thalamus: the midline nuclei. *Prog. Brain. Res*. 87, 53–80.

Berendse, H.W., and Groenewegen, H.J. (1990). Organization of the thalamostriatal projections in the rat, with special emphasis on the ventral striatum. *J. Comp. Neurol.* 299, 187–228.

Chen, B., Schaevitz, L.R., McConnell, S.K. (2005). Fezl regulates the differentiation and axon targeting of layer 5 subcortical projection neurons in cerebral cortex. *Proc. Natl. Acad. Sci.* USA 102, 17184–17189.

Cowan, R.L., Wilson, C.J., Emson, P.C., Heizmann, C.W. (1990). Parvalbumin-containing GABAergic interneurons in the rat neostriatum. *J. Comp. Neurol.* 302, 197–205.

DeFelipe, J. (1993). A study of NADPH diaphorase-positive axonal plexuses in the human temporal cortex. *Brain Res.* 615, 342–346.

Ding, J., Peterson, J.D., Surmeier, D.J. (2008). Corticostriatal and thalamostriatal synapses have distinctive properties. *J. Neurosci.* 28, 6483–6492.

Ding, J.B., Guzman, J.N., Peterson, J.D., Goldberg, J.A., Surmeier, D.J. (2010). Thalamic gating of corticostriatal signaling by cholinergic interneurons. *Neuron.* 67, 294–307.

Dougherty, R.P. (2005). Extensions of DAMAS and benefits and limitations of deconvolution in beamforming. *AIAA Paper*. 2005-2961.

Doyon, J., Bellec, P., Amsel, R., Penhune, V., Monchi, O., Carrier, J., et al. (2009). Contributions of the basal ganglia and functionally related brain structures to motor learning. *Behav. Brain. Res.* 199, 61–75.

Dubé, L., Smith, A.D., Bolam, J.P. (1988). Identification of synaptic terminals of thalamic or cortical origin in contact with distinct medium-size spiny neurons in the rat neostriatum. *J. Comp. Neurol.* 267, 455–471.

Ellender, T.J., Harwood, J., Kosillo, P., Capogna, M., Bolam, J.P. (2013). Heterogeneous properties of central lateral and parafascicular thalamic synapses in the striatum. *J. Physiol.* 591, 257–272.

English, D.F., Ibanez-Sandoval, O., Stark, E., Tecuapetla, F., Buzski, G., Deisseroth, K., et al. (2012). GABAergic circuits mediate the reinforcement-related signals of striatal cholinergic interneurons. *Nat. Neurosci.* 15, 123130.

Erro, M.E., Lanciego, J.L., Arribas, J., Giménez-Amaya, J.M. (2001). Striatal input from the ventrobasal complex of the rat thalamus. *Histochem. Cell. Biol.* 115, 447–54.

Fremeau, R.T., Voglmaier, S., Seal, R.P., Edwards, R.H. (2004). VGLUTs define subsets of excitatory neurons and suggest novel roles for glutamate. *Trends. Neurosci.* 27, 98–103.

Frotscher, M., Rinne, U., Hassler, R., Wagner, A. (1981). Termination of cortical afferents on identified neurons in the caudate nucleus of the cat. *Exp. Brain. Res.* 41, 329–337.

Fujiyama, F., Furuta, T., Kaneko, T. (2001). Immunocytochemical localization of candidates for vesicular glutamate transporters in the rat cerebral cortex. *J. Comp. Neurol.* 435, 379–387.

Fujiyama, F., Unzai, T., Nakamura, K., Nomura, S., Kaneko, T. (2006). Difference in organization of corticostriatal and thalamostriatal synapses between patch and matrix compartments of rat neostriatum. *Eur. J. Neurosci.* 24, 2813–2824.

Garas, F.N., Shah, R.S., Kormann, E., Doig, N.M., Vinciati, F., Nakamura, K.C., et al. (2016). Secretagogin expression delineates functionally-specialized populations of striatal parvalbumin-containing interneurons. *eLife*. 5. pii: e16088.

Gittis, A.H., Hang, G.B., LaDow, E.S., Shoenfeld, L.R., Atallah, B.V., Finkbeiner, S., et al. (2011). Rapid target-specific remodeling of fast-spiking inhibitory circuits after loss of dopamine. *Neuron*. 71, 858–868.

Gittis, A.H., Nelson, A.B., Thwin, M.T., Palop, J.J., Kreitzer, A.C. (2010). Distinct roles of GABAergic interneurons in the regulation of striatal output pathways. *J. Neurosci*. 30, 2223–2234.

Graybiel, A.M. (2005). The basal ganglia: learning new tricks and loving it. *Curr. Opin. Neurobiol*. 15, 638–644.

Groenewegen, H.J., and Berendse, H.W. (1994). The specificity of the "nonspecific" midline and intralaminar thalamic nuclei. *Trends. Neurosci*. 17, 52–57.

Gustafson, N., Gireesh-Dharmaraj, E., Czubayko, U., Blackwell, K., Plenz, D. (2006) A comparative voltage and current-clamp analysis of feedback and feedforward synaptic transmission in the striatal microcircuit in vitro. *J. Neurophy*s. 95, 737-752

Haber, S., and McFarland, N.R. (2001). The place of the thalamus in frontal cortical-basal ganglia circuits. *Neurosci*. 7, 315–324.

Hattori, T., McGeer, E.G., McGeer, P.L. (1979). Fine structural analysis of the cortico-striatal pathway. *J. Comp. Neurol*. 185, 347–353.

Hazlett, J.C., and Bagley, S.D. (1983). Origin and topography of thalamocaudate projections in the opossum. *Neurosci. Lett*. 36, 19–24.

Hersch, S.M., Ciliax, B.J., Gutekunst, C.A., Rees HD, Heilman CJ, Yung KK, et al. (1995). Electron microscopic analysis of D1 and D2 dopamine receptor proteins in the dorsal striatum and their synaptic relationships with motor corticostriatal afferents. *J. Neurosci*. 15, 5222–5237.

Hikosaka, O., Nakamura, K., Sakai, K., Nakahara, H. (2002). Central mechanisms of motor skill learning. *Curr. Opin. Neurobio*l. 12, 217–222.

Hikosaka, O., Takikawa, Y., Kawagoe, R. (2000). Role of the basal ganglia in the control of purposive saccadic eye movements. *Physiol. Rev.* 80, 953–978.

Hisano, S., Hoshi, K., Ikeda, Y., Maruyama, D., Kanemoto, M., Ichijo, H., et al. (2000). Regional expression of a gene encoding a neuron-specific Na(+)-dependent inorganic phosphate cotransporter (DNPI) in the rat forebrain. *Mol. Brain. Res*. 83, 34–43.

Holderith, N., Lorincz, A., Katona, G., Rózsa, B., Kulik, A., Watanabe, M., et al. (2012). Release probability of hippocampal glutamatergic terminals scales with the size of the active zone. *Nat. Neurosci.* 15, 988–997.

Hontanilla, B., Parent, A., Giménez-Amaya, J.M. (1997). Parvalbumin and calbindin D-28k in the entopeduncular nucleus, subthalamic nucleus, and substantia nigra of the rat as revealed by double-immunohistochemical methods. *Synapse*. 25, 359–367.

Huerta-Ocampo, I., Mena-Segovia, J., Bolam, J.P. (2014). Convergence of cortical and thalamic input to direct and indirect pathway medium spiny neurons in the striatum. *Brain. Struct. Funct.* 219, 1787–1800.

Ibáñez-Sandoval, O., Tecuapetla, F., Unal, B., Shah, F., Koós, T., Tepper, J.M. (2011). A novel functionally distinct subtype of striatal neuropeptide Y interneuron. *J. Neurosci*. 31, 16757–16769.

Ichinohe, N., Iwatsuki, H., Shoumura, K. (2001). Intrastriatal targets of projection fibers from the central lateral nucleus of the rat thalamus. *Neurosci. Lett*. 302, 105–108.

Inase, M., Sakai, S.T., Tanji, J. (1996). Overlapping corticostriatal projections from the supplementary motor area and the primary motor cortex in the macaque monkey: an anterograde double labeling study. *J. Comp. Neurol*. 373, 283–296.

Jones EG. (2007). *The Thalamus.* 2nd ed. Cambridge University Press. Cambridge, UK.

Kachidian, P., Vuillet, J., Nieoullon, A., et al. (1996). Striatal neuropeptide Y neurones are not a target for thalamic afferent fibres. *Neuroreport.* 7, 1665–1669.

Kameda, H., Furuta, T., Matsuda, W., Ohira, K., Nakamura, K.C., Hioki, H., et al. (2008). Targeting green fluorescent protein to dendritic membrane in central neurons. *Neurosci. Res*. 61, 79-91.

Kameda, H., Hioki, H., Tanaka, Y.H., Tanaka, T., Sohn, J., Sonomura, T., et al. (2012). Parvalbumin-producing cortical interneurons receive inhibitory inputs on proximal portions and cortical excitatory inputs on distal dendrites. *Eur. J. Neurosci*. 35, 838–854.

Kaneko, T., and Fujiyama, F. (2002). Complementary distribution of vesicular glutamate transporters in the central nervous system. *Neurosci. Res*. 42, 243–250.

Kaneko, T., Fujiyama, F., Hioki, H. (2002). Immunohistochemical localization of candidates for vesicular glutamate transporters in the rat brain. *J. Comp. Neurol*. 444, 39–62.

Kawaguchi, Y. (1993). Physiological, morphological, and histochemical characterization of three classes of interneurons in rat neostriatum. *J. Neurosci*. 13, 4908–4923.

Kawaguchi, Y., Wilson, C.J., Augood, S.J., Emson, P.C. (1995). Striatal interneurons - chemical, physiological and morphological characterization. *Trends. Neurosci*. 18, 527–535.

Kemp, J.M., and Powell, T.P.S. (1971). The synaptic organization of the caudate nucleus. *Phil. Trans. Roy. Soc. L. B*. 262, 403–412.

Kincaid, A.E., Zheng, T., Wilson, C.J. (1998). Connectivity and convergence of single corticostriatal axons. *J. Neurosci*. 18, 4722-4731.

Kita, H., Kosaka, T., Heizmann, C.W. (1990). Parvalbumin-immunoreactive neurons in the rat neostriatum: a light and electron microscopic study. *Brain. Res*. 536, 1–15.

Klausberger, T., and Somogyi, P. (2008). Neuronal diversity and temporal dynamics: the unity of hippocampal circuit operations. *Science*. 321, 53–57.

Koos, T., Tepper, J.M., Wilson, C.J. (2004). Comparison of IPSCs evoked by spiny and fast-spiking neurons in the neostriatum. *J. Neurosci*. 24, 7916–7922.

Koos, T., Tepper, J.M. (1999). Inhibitory control of neostriatal projection neurons by GABAergic interneurons. *Nat. Neurosci*. 2, 467–472.

Kosaka, T., Yasuda, S., Kosaka, K. (2017). Calcium-binding protein, secretagogin, characterizes novel groups of interneurons in the rat striatum. *Neurosci. Res*. 119, 53–60.

Kress, G.J., Yamawaki, N., Wokosin, D.L., Wickersham, I.R., Shepherd, G.M.G., Surmeier, D.J. (2013). Convergent cortical innervation of striatal projection neurons. *Nature Neurosci*. 16, 665- 667.

Kubota, Y., and Kawaguchi, Y. (1994). Three classes of GABAergic interneurons in neocortex and neostriatum. *Jpn. J. Physiol.* 44 Suppl 2, S145-148.

Kubota, Y., and Kawaguchi, Y. (1993). Spatial distributions of chemically identified intrinsic neurons in relation to patch and matrix compartments of rat neostriatum. *J. Comp. Neurol.* 332, 499–513.

Kubota, Y., and Kawaguchi, Y. (2000). Dependence of GABAergic synaptic areas on the interneuron type and target size. *J. Neurosci.* 20, 375–386.

Kubota, Y., Mikawa, S., Kawaguchi, Y. (1993). Neostriatal GABAergic interneurones contain NOS, calretinin or parvalbumin. *Neuroreport.* 5, 205–208.

Kunishio, K., Haber, S.N. (1994). Primate cingulostriatal projection: Limbic striatal versus sensorimotor striatal input. *J. Comp. Neurol.* 350, 337–356.

Kuramoto, E., Fujiyama, F., Nakamura, K.C., Tanaka, Y., Hioki, H., Kaneko, T. (2011). Complementary distribution of glutamatergic cerebellar and GABAergic basal ganglia afferents to the rat motor thalamic nuclei. *Eur. J. Neurosci.* 33, 95–109.

Kuramoto, E., Furuta, T., Nakamura, K.C., Unzai, T., Hioki, H., Kaneko, T. (2009). Two types of thalamocortical projections from the motor thalamic nuclei of the rat: A single neuron-tracing study using viral vectors. *Cereb. Cortex.* 19, 2065–2077.

Kuramoto, E., Ohno, S., Furuta, T., Unzai, T., Tanaka, Y.R., Hioki, H., et al. (2015). Ventral medial nucleus neurons send thalamocortical afferents more widely and more preferentially to layer 1 than neurons of the ventral anterior-ventral lateral nuclear complex in the rat. *Cereb. Cortex.* 25, 221–235.

Lacey, C.J., Boyes, J., Gerlach, O., Chen, L., Magill, P.J., Bolam, J.P. (2005). GABA(B) receptors at glutamatergic synapses in the rat striatum. *Neuroscience*. 136, 1083–1095.

Lacey, C.J., Bolam, J.P., Magill, P.J. (2007). Novel and distinct operational principles of intralaminar thalamic neurons and their striatal projections. *J. Neurosci*. 27, 4374–84.

Lapper, S.R., and Bolam, J.P. (1992). Input from the frontal cortex and the parafascicular nucleus to cholinergic interneurons in the dorsal striatum of the rat. *Neuroscience*. 51, 533–545.

Lapper, S.R., Smith, Y., Sadikot, A.F., Parent, A., Bolam, J.P. (1992). Cortical input to parvalbumin-immunoreactive neurones in the putamen of the squirrel monkey. *Brain Res*. 580, 215–224.

Lee, C.C., and Sherman, S.M. (2008). Synaptic properties of thalamic and intracortical inputs to layer 4 of the first- and higher-order cortical areas in the auditory and somatosensory systems. *J. Neurophysiol*. 100, 317–326.

Lee, C.C., and Sherman, S.M. (2010). Drivers and modulators in the central auditory pathways. *Frontiers in Neurosci*. 4, 79-96.

Lei, W., Jiao, Y., Del Mar, N., Reiner, A. (2004). Evidence for differential cortical input to direct pathway versus indirect pathway striatal projection neurons in rats. *J. Neurosci*. 24, 8289–8299.

Lei, W., Deng, Y., Liu, B., Mu, S., Guley, N.M., Wong, T., et al. (2013). Confocal laser scanning microscopy and ultrastructural study of VGLUT2 thalamic input to striatal projection neurons in rats. *J. Comp. Neurol*. 521, 1354–1377.

Lindström, S., and Wróbel, A. (1990). Frequency dependent corticofugal excitation of principal cells in the cat's dorsal lateral geniculate nucleus. *Exp. Brain. Res*. 79, 313–318.

Liu, B., Ouyang, L., Mu, S., Zhu, Y., Li, K., Zhan, M., et al. (2011). The morphological characteristics of corticostriatal and thalamostriatal neurons and their intrastriatal terminals in rats. *Surg. Radiol. Anat*. 33, 807–817.

Lorente de Nó, R. (1992). The cerebral cortex of the mouse (a first contribution - the "acoustic" cortex). *Somatosens. Mot. Res*. 9, 3–36.

Mackenzie, P.J., Kenner, G.S., Prange, O., Shayan, H., Umemiya, M., Murphy, T.H. (1999). Ultrastructural correlates of quantal synaptic function at single CNS synapses. *J. Neurosci*. 19, 1-7.

Mallet, N., Ballion, B., Le, Moine, C., Gonon, F. (2006) Cortical inputs and GABA interneurons imbalance projection neurons in the striatum of parkinsonian rats. *J. Neurosci*. 26, 3875-3884.

Mao, T., Kusefoglu, D., Hooks, B.M., Huber, D., Petreanu, L., Svoboda, K. (2011) Long-range neuronal circuits underlying the interaction between sensory and motor cortex. *Neuron* 72, 111-23.

McFarland, N.R., and Haber, S.N. (2001). Organization of thalamostriatal terminals from the ventral motor nuclei in the macaque. *J. Comp. Neurol*. 429, 321–336.

McFarland, N.R., and Haber, S.N. (2000). Convergent inputs from thalamic motor nuclei and frontal cortical areas to the dorsal striatum in the primate. *J. Neurosci*. 20, 3798–813.

Mengual, E., De Las Heras, S., Erro, E., et al. (1999). Thalamic interaction between the input and the output systems of the basal ganglia. *J. Chem. Neuroanat*. 16, 185–197.

Miyamoto, Y., and Fukuda, T. (2015.) Immunohistochemical study on the neuronal diversity and three-dimensional organization of the mouse entopeduncular nucleus. *Neurosci. Res.* 94, 37–49.

Molyneaux, B.J., Arlotta, P., Menezes, J.R., Macklis, J.D. (2007). Neuronal subtype specification in the cerebral cortex. *Nat. Rev. Neurosci.* 8, 427–437.

Morishima, M., and Kawaguchi, Y. (2006). Recurrent connection patterns of corticostriatal pyramidal cells in frontal cortex. *J. Neurosci.* 26, 4394-405.

Muñoz-Manchado, A.B., Foldi, C., Szydlowski, S., Sjulson, L., Farries, M., Wilson, C., et al. (2016). Novel striatal GABAergic interneuron populations labeled in the 5ht3aegfp mouse. *Cereb. Cortex.* 26, 96–105.

Norenberg, A., Hu, H., Vida, I., Bartos, M., Jonas, P., et al. (2010). Distinct nonuniform cable properties optimize rapid and efficient activation of fast-spiking GABAergic interneurons. *Proc. Natl. Acad. Sci. USA.* 107, 894–899.

Nusser, Z., Cull-Candy, S., Farrant, M. (1997). Differences in synaptic GABA(A) receptor number underlie variation in GABA mini amplitude. *Neuron.* 19, 697–709.

Parent, A., and De Bellefeuille, L. (1983). The pallidointralaminar and pallidonigral projections in primate as studied by retrograde double-labeling method. *Brain Res.* 278, 11–27.

Parent, A., and Hazrati, L.N. (1995). Functional anatomy of the basal ganglia. II. The place of subthalamic nucleus and external pallidium in basal ganglia circuitry. *Brain Res. Rev.* 20, 128–154.

Paxinos, G., Franklin, K.B.J. (2013). *The mouse brain in stereotaxic coordinates*. 4th Ed. Elsevier: Academic Press, London, UK.

Planert, H., Szydlowski, S.N., Hjorth, J.J.J., Grillner, S., Silberberg, G. (2010). Dynamics of synaptic transmission between fast-spiking interneurons and striatal projection neurons of the direct and indirect pathways. J. Neurosci. 30, 3499–3507.

Raju, D.V., Shah, D.J., Wright, T.M., Hall, R.A., Smith, Y. (2006). Differential synaptology of vGluT2-containing thalamostriatal afferents between the patch and matrix compartments in rats. *J. Comp. Neurol*. 499, 231–243.

Ramanathan, S., Hanley, J.J., Deniau, J., Bolam, J.P. (2002). Synaptic convergence of motor and somatosensory cortical afferents onto GABAergic Interneurons in the rat striatum. *J. Neurosci*. 22, 8158–8169.

R Core Team, (2015). R: A Language and Environment for Statistical Computing

Reiner, A., Jiao, Y., Del, Mar, N., Laverghetta, A.V., Lei, W.L. (2003) Differential morphology of pyramidal tract-type and intratelencephalically projecting-type corticostriatal neurons and their intrastriatal terminals in rats. *J Comp Neurol* 457:420–440.

Reiner, A., Hart, N.M., Lei, W., Deng, Y. (2010). Corticostriatal projection neurons - dichotomous types and dichotomous functions. *Front. Neuroanat.* 4, 142.

Rudkin, T.M., and Sadikot, A.F. (1999). Thalamic input to parvalbumin-immunoreactive GABAergic interneurons: Organization in normal striatum and effect of neonatal decortication. *Neuroscience*. 88, 1165–1175.

Sadikot, A.F., Parent, A., Smith, Y., Bolam, J.P. (1992). Efferent connections of the centromedian and parafascicular thalamic nuclei in the squirrel monkey: A light and electron

microscopic study of the thalamostriatal projection in relation to striatal heterogeneity. *J. Comp. Neurol*. 320, 228–242.

Saiki, A., Kimura, R., Samura, T., Fujiwara-Tsukamoto, Y., Sakai, Y., Isomura, Y. (2014). Different modulation of common motor information in rat primary and secondary motor cortices. *PLoS ONE*. 9: e98662.

Schindelin, J., Arganda-Carreras, I., Frise, E., Kaynig, V., Longair, M., Pietzsch, T., et al. (2012). Fiji: an open-source platform for biological-image analysis. *Nat. Methods*. 9, 676-682.

Sciamanna, G., Ponterio, G., Mandolesi, G., Bonsi, P., Pisani, A. (2015). Optogenetic stimulation reveals distinct modulatory properties of thalamostriatal vs corticostriatal glutamatergic inputs to fast-spiking interneurons. *Sci. Rep*. 5: 16742.

Shepherd, G.M. (2013). Corticostriatal connectivity and its role in disease. *Nat. Rev. Neurosci*.14, 278-291.

Shermann, S.M., and Guillery, R.W. (1998). On the actions that one nerve cell can have on another: Distinguishing ''drivers'' from ''modulators''. *Proc. Natl. Acad. Sci*. 95, 7121–7126,

Sidibe, M., and Smith, Y. (1999). Thalamic inputs to striatal interneurons in monkeys: Synaptic organization and co-localization of calcium binding proteins. *Neuroscience*. 89, 1189–1208.

Smeal, R.M., Gaspar, R.C., Keefe, K.A., Wilcox, K.S. (2007). A rat brain slice preparation for characterizing both thalamostriatal and corticostriatal afferents. *J. Neurosci. Methods*. 159, 224–235.

Smith, Y., Bennett, B.D., Bolam, J.P., Parent, A., Sadikot, A.F. (1994). Synaptic relationships between dopaminergic afferents and cortical or thalamic input in the sensorimotor territory of the striatum in monkey. *J. Comp. Neurol.* 344, 1–19.

Smith, Y., and Bolam, J.P. (1990). The output neurones and the dopaminergic neurones of the substantia nigra receive a GABA-containing input from the globus pallidus in the rat. *J. Comp. Neurol.* 296, 47–64.

Smith, Y., Parent, A. (1986). Differential connections of caudate nucleus and putamen in the squirrel monkey (Saimiri sciureus). *Neuroscience.* 18, 347–371.

Smith, Y., Raju, D.V., Pare, J.F., Sidibe, M. (2004). The thalamostriatal system: A highly specific network of the basal ganglia circuitry. *Trends. Neurosci.* 27, 520–527.

Somogyi, P., Bolam, J.P., Smith, A.D. (1981). Monosynaptic cortical input and local axon collaterals of identified striatonigral neurons. A light and electron microscopic study using the Golgi-peroxidase transport-degeneration procedure. *J. Comp. Neurol.* 195, 567–584.

Stern, E.A., Jaeger, D., Wilson, C.J. (1998). Membrane potential synchrony of simultaneously recorded striatal spiny neurons in vivo. *Nature.* 394, 475-478.

Stevens, C.F. (2003). Neurotransmitter release at central synapses. *Neuron.* 40, 381-388.

Straub, C., Saulnier, J.L., Feng, D.D., Huang, K.W., Sabatini, B.L. (2016). Principles of synaptic organization of GABAergic interneurons in the striatum report principles of synaptic organization of GABAergic interneurons in the striatum. *Neuron.* 92, 84–92.

Sul, J.H., Jo, S., Lee, D., Jung, M.W. (2011). Role of rodent secondary motor cortex in value-based action selection. *Nature Neurosci.* 14, 1202-1208.

Takada, M., Itoh, K., Sugimoto, T., Mizuno, N. (1985a). Topographical projections from the thalamus to the putamen in the cat. *Neurosci. Lett*. 54, 207–212.

Takada, M., Itoh, K., Yasui, Y., Sugimoto, T., Mizuno, N. (1985b). Topographical projections from the posterior thalamic regions to the striatum in the cat, with reference to possible tecto-thalamo-striatal connections. *Exp. Brain. Res*. 60, 385–396.

Takada, M., Tokuno, H., Nambu, A., Inase, M. (1998). Corticostriatal input zones from the supplementary motor area overlap those from the contra-rather than ipsilateral primary motor cortex. *Brain Res*. 791, 335–340.

Tanaka, J., Matsuzaki, M., Tarusawa, E., Momiyama, A., Molnar, E., Kasai, H., et al. (2005). Number and density of AMPA receptors in single synapses in immature cerebellum. *J. Neurosci.* 25, 799–807.

Tepper, J.M., and Bolam, J.P. (2004). Functional diversity and specificity of neostriatal interneurons. *Curr. Opin. Neurobiol*. 14, 685–692.

Tepper, J.M., Tecuapetla, F., Koós, T., Ibáñez-Sandoval, O. (2010). Heterogeneity and diversity of striatal GABAergic interneurons. *Front. Neuroanat*. 4,150.

Timofeev, I., and Steriade, M. (1997). Fast (mainly 30-100 Hz) oscillations in the cat cerebellothalamic pathway and their synchronization with cortical potentials. *J. Physiol*. 504, 153–168.

Turner, J.P., and Salt, T.E. (1998). Characterization of sensory and corticothalamic excitatory inputs to rat thalamocortical neurones in vitro. *J. Physiol*. 510, 829–843.

Ueta, Y., Hirai, Y., Otsuka, T., Kawaguchi, Y. (2013). Direction- and distance-dependent interareal connectivity of pyramidal cell subpopulations in the rat frontal cortex. *Front. Neural. Circuits*. 7, 164.

Unzai, T., Kuramoto, E., Kaneko, T., Fujiyama, F. (2015). Quantitative analyses of the projection of individual neurons from the midline thalamic nuclei to the striosome and matrix compartments of the rat striatum. *Cereb. Cortex*. 27, 1164-1181.

Van Der Werf, Y.D., Witter, M.P., Groenewegen, H.J. (2002). The intralaminar and midline nuclei of the thalamus. Anatomical and functional evidence for participation in processes of arousal and awareness. *Brain Res. Rev*. 39, 107–140.

Veening, J.G., Cornelissen, F.M., Lieven, P.A.J.M. (1980). The topical organization of the afferents to the caudatoputamen of the rat. A horseradish peroxidase study. *Neuroscience*. 5, 1253–1268.

Vincent, S.R., and Johansson, O. (1983). Striatal neurons containing both somatostatin- and avian pancreatic polypeptide (APP)-like immunoreactivities and NADPH-diaphorase activity: A light and electron microscopic study. *J. Comp. Neurol*. 217, 264–270.

Vincent, S.R., Satoh, K., Armstrong, D.M., Fibiger, H.C. (1983). Substance P in the ascending cholinergic reticular system. *Nature*. 306, 688–691.

von Krosigk, M., Monckton, J.E., Reiner, P.B., McCormick, D.A. (1999). Dynamic properties of corticothalamic excitatory postsynaptic potentials and thalamic reticular inhibitory postsynaptic potentials in thalamocortical neurons of the guinea-pig dorsal lateral geniculate nucleus. *Neuroscience*. 91, 7–20.

Voorn, P., Vanderschuren, L.J.M.J., Groenewegen, H.J., Robbins, T.W., Pennartz, C.M.A. (2004). Putting a spin on the dorsal-ventral divide of the striatum. *Trends. Neurosci*. 27, 468–474.

Vuillet, J., Kerkerian, L., Kachidian, P., Bosler, O., Nioeullon, A. (1989). Ultrastructural correlates of functional relationships between nigral dopaminergic or cortical afferent fibers and neuropeptide Y-containing neurons in the rat striatum. *Neurosci. Lett*. 100, 99–104.

Wheeler, D.W., White, C.M., Rees, C.L., Komendantov, A.O., Hamilton, D.J., Ascoli, G.A. (2015). Hippocampome.org: A knowledge base of neuron types in the rodent hippocampus. *Elife.* 4. pii: e09960.

Wictorin, K., Ouimet, C.C., Björklund, A. (1989). Intrinsic organization and connectivity of intrastriatal striatal transplants in rats as revealed by DARPP-32 immunohistochemistry: specificity of connections with the lesioned host brain. *Eur. J. Neurosci*. 1, 690–701.

Wilson, C.J. (1987). Morphology and synaptic connections of crossed corticostriatal neurons in the rat. *J. Com. Neurol*. 263, 567-580.

Wilson, C.J. (1992). Dendritic morphology, inward rectification, and the functional properties of neostriatal neurons. In *Single neuron computation,* eds. McKenna T, Davis J, Zornetzer S., Chapter 6. Paris: Academic Press.

Wilson, C.J., Groves, P.M. (1981). Spontaneous firing patterns of identified spiny neurons in the rat neostriatum. *Brain Res*. 220, 67-80.

Wilson, C.J., Xu, Z.C., Emson, P.C., Feler, C. (1990). Anatomical and physiological properties of the cortical and thalamic innervations of neostriatal tissue grafts. *Prog. Brain. Res*. 82, 417–426.

Xu, Z.C., Wilson, C.J., Emson, P.C. (1989). Restoration of the corticostriatal projection in rat neostriatal grafts: electron microscopic analysis. *Neuroscience*. 29, 539–550.

Xu, Z.C., Wilson, C.J., Emson, P.C. (1991). Synaptic potentials evoked in spiny neurons in rat neostriatal grafts by cortical and thalamic stimulation. *J. Neurophysiol*. 65:477–93.
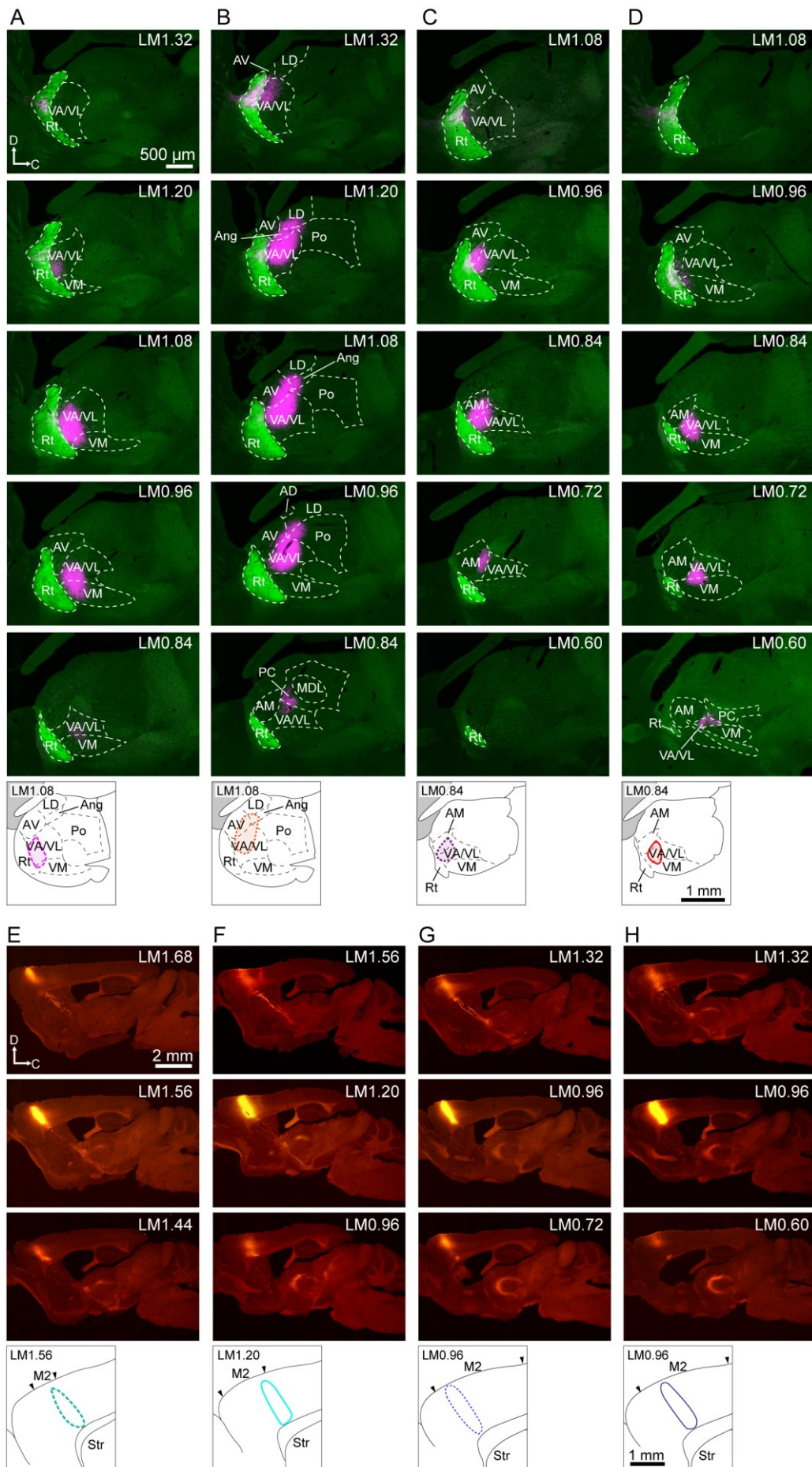
Supplementary Fig.1. Verification of the infected neurons following AAV injection into the VA/VL and M2. **A-D**. Images showing the viral injection site in the ventral thalamus. Subnuclei of the thalamus are identified with PV-GFP immunoreactivity (green). VA/VL is located on the caudal side of Rt immunoreactive for PV-GFP. Mice A and D were used for the apposition analysis. **E-H**. Images showing the viral injection site in the M2. AAV injection site was centered in M2 (LM 0.96-1.56 mm, middle row) and the infected neurons was extent from LM0.60 to 1.68 mm, corresponding to mainly M2 but a little M1 area. Mice F, G, and H were used for the apposition analysis. Photos were acquired with an epifluorescent microscope (BX-53, Olympus, Tokyo, Japan) under the conditions described in the Materials and Methods section. AM, anteromedial thalamic nucleus; Po, posterior thalamic nuclear group; Rt, reticular nucleus (prethalamus); VA/VL, ventral anterior / ventral lateral complex; VM, ventromedial thalamic nucleus (Paxinos and Franklin, 2013). For each injection case, different colors of lines and shades are used. The red color group is for thalamic injections and blue color group for cortical injections. Color code is the same as in Figure 3.